Shock compaction heating and collisional processes in the production of type 3 ordinary chondrites: Lessons from the (nearly) unique L3 chondrite melt breccia Northwest Africa 8709*

Journal Item

Shock compaction heating and collisional processes in the production of type 3 ordinary chondrites: Lessons from the (nearly) unique L3 chondrite melt breccia Northwest Africa 8709*

Alex M. Ruzicka[1 †], Jon M. Friedrich[2,3], Melinda L. Hutson[1], Juliette W. Strasser[2], Robert J. Macke[4], Mark L. Rivers[5], Richard C. Greenwood[6], Karen Ziegler[7], and Richard N. Pugh[1]

[1] Portland State University, Department of Geology and Cascadia Meteorite Laboratory, 17 Cramer Hall, 1721 SW Broadway, Portland, OR, USA

[2] Department of Chemistry, Fordham University, 441 East Fordham Road, Bronx, NY 10458

[3] Department of Earth and Planetary Sciences, American Museum of Natural History, 79th Street at Central Park West, New York, NY 10024

[4] Vatican Observatory, V-00120, Vatican City-State

[5] Center for Advanced Radiation Sources, University of Chicago, Argonne, Illinois 60439

[6] Planetary Sciences Research Institute, The Open University, Walton Hall, Milton Keynes, MK7 6AA, UK

[7] Institute of Meteoritics, University of New Mexico, Albuquerque, NM 87131

Revised July 30, 2020

Submitted to *Meteoritics & Planetary Science*

†Corresponding Author. tel: 503-725-3372; fax:503-725-3025; e-mail: ruzickaa@pdx.edu

* This paper is dedicated to the memory of Richard ("Dick") Pugh, who passed away during peer review. The NWA 8709 stone was found and purchased by Dick in a local rock shop in Portland, Oregon, U.S.A., and shortly thereafter recognized as unusual and significant.

Abstract. Northwest Africa (NWA) 8709 is a rare example of a type 3 ordinary chondrite melt breccia and provides critical information for the shock compaction histories of chondrites. An L3 protolith for NWA 8709 is inferred on the basis of oxygen isotope composition, elemental composition, diverse mineral chemistry, and overall texture. NWA 8709 is among the most strongly shocked type 3 chondrites known, and experienced complete melting of the matrix and partial melting of chondrules. Unmelted phases underwent FeO-reduction and partial homogenization, with reduction possibly occurring by reaction of olivine and low-Ca pyroxene with an S-bearing gas that was produced by vaporization. Chondrules and metal grains became foliated by uniaxial compaction, and during compression, chondrules and fragments became attached to form larger clumps. This process, and possibly also melt incorporation into chondrules to cause 'inflation', may have contributed to anomalously large chondrule sizes in NWA 8709. The melt breccia character is attributed to strong shock affecting a porous precursor. Data-model comparisons suggest that a precursor with 23% porosity that was impacted by a 3 km/s projectile could have produced the meteorite. The rarity of other type 3 ordinary chondrite melt breccias implies that the immediate precursors to such chondrites were lower in porosity than the NWA 8709 precursor, or experienced weaker shocks. Altogether, the data imply a predominantly 'quiet' dynamical environment to form most type 3 ordinary chondrites, with compaction occurring in a series of relatively weak shock events.

INTRODUCTION

Northwest Africa (NWA) 8709 is classified as an L3 melt breccia, consisting of chondrules and fragments set in an igneous-textured matrix (MBD, 2019). Such melt breccias are rare among ordinary chondrites, especially weakly-metamorphosed (type 3) ordinary chondrites such as NWA 8709. Using recent (October, 2019) data for classified meteorites from the

Meteoritical Bulletin Database (MBD), recognized melt breccias constitute 0.26% (134 of 51,725) of all ordinary chondrites, and 0.10% (only 3 of 3028) of type 3 ordinary chondrites (Table 1). Despite their rarity, melt breccias provide unique information for shock-processing, impact histories, and compaction processes that contributed to the lithification of what are expected to have been initially porous primordial chondritic agglomerates (Bland et al., 2014). We studied the petrography, chemistry, and structure of NWA 8709 with optical microscopy (OM), scanning electron microcopy (SEM), inductively-coupled-plasma - mass-spectrometry (ICP-MS), microtomography (μCT), ideal gas pycnometry, and oxygen isotope analyses to better understand the physical, chemical, and thermal processes involved in forming chondritic melt breccias and the conditions needed to create them. A preliminary report on NWA 8709 was given by Ruzicka et al. (2015a).

SAMPLES AND METHODS

All data for NWA 8709 were obtained on a single specimen (curated at the Cascadia Meteorite Laboratory—CML) whose original mass is estimated to have been ~79 g. Two polished thin sections (CML0109-2 and -5D) of NWA 8709 were studied by OM and with a Zeiss Sigma SEM at Portland State University, to obtain petrographic and mineral-chemical data, including the determination of textures, shock stages, and quantitative phase compositions using SEM, largely following the methods of Ruzicka et al. (2017). We also used OM to measure chondrule sizes in the two thin sections, taking the diameter to be the average of length and width. A 2.2-2.3 g piece of the meteorite (CML0109-5C) was studied for both μCT and for dedicated bulk density-porosity measurements. Microtomography data were obtained at an image resolution of 8.24 μm/voxel (a voxel is a 3D volume element akin to a 2D pixel) using the methods and apparatus described in Ebel and Rivers (2007), and together with other methods

described in an electronic annex (see Supplemental Materials), were used to provide information on chondrule shapes, sizes and orientations, and on the orientations of metal grains. Dedicated bulk density-porosity measurements were obtained using measured sample mass and a NextEngine model 2020i HD-Pro laser scanner, which creates a computer model of the sample from which the volume is calculated, and grain volume determined using ideal-gas (N_2) pycnometry using a Quantachrome Ultrapycnometer 1000. Five aliquots of NWA 8709 (120.6 mg, 117.2 mg, 106.0 mg, 93.2 mg, 72.1 mg) from samples CML0109-5A and -5B were analyzed with a ThermoElemental X-Series II ICPMS at Fordham University using the methods outlined in Friedrich et al. (2003) and Wolf et al. (2012), to obtain a total of 53 quantified trace, minor, and major elements. An aliquot of sample CML0109-1 was analyzed for oxygen isotope composition at the Open University, Planetary Sciences Research Institute, using infrared (10 μm wavelength) laser-assisted fluorination coupled with high-mass-resolution mass spectrometry, following the procedures of Miller et al. (1999), with system precision (2σ) for $\delta^{17}O$, $\delta^{18}O$, and $\Delta^{17}O$ (= $\delta^{17}O - 0.52\ \delta^{18}O$) estimated as ±0.05‰, ±0.09‰, and ±0.02‰, respectively. Three aliquots of another sample, CML0109-7, were analyzed for oxygen isotope composition at the University of New Mexico, Institute of Meteoritics, by laser fluorination of acid-washed samples, following the procedures outlined by Agee et al. (2013). Other details about methods and instrumentation for optical microscopy, SEM, and microtomography are provided in Supplemental Materials.

RESULTS

Texture and mineralogy

Figures 1-3 illustrate petrographic features of NWA 8709. Large-scale features are shown in Fig. 1, details of chondrule textures in Fig. 2, and details of matrix textures in Fig. 3.

In cut faces and in thin section, NWA 8709 shows numerous chondrules set in a fine-grained, opaque matrix (Fig. 1), in this way resembling a type 3 ordinary chondrite. Chondrules appear aligned (Fig. 1a), and are tightly packed (Fig. 1b-d). Some chondrules are in direct contact with nearest neighbors and have shapes that conform to these neighbors. For instance, in Fig. 1b, cryptocrystalline chondrule C appears to be partly draped around barred pyroxene-olivine chondrule B1. In Fig. 1c-d, three fine-grained pyroxene-rich chondrules (A, B, C) have been molded together with an olivine-pyroxene microporphyry chondrule (D). No matrix separates these chondrules; instead, metal (or weathered metal) and sulfide or simply a textural discontinuity occurs at the joins between these chondrules. In Fig. 2e, three pyroxene-rich chondrules (A, B, C) are in direct contact with one another. In Fig. 2f, microporphyritic chondrules A1 and B form a tight fit.

The most distinctive feature of NWA 8709, and the one that makes it a melt breccia, is the presence of an igneous-textured melt matrix between chondrules (Fig. 1b, 2d-f, 3a-d). This matrix is composed of fine-grained (≤5 μm across) silicates including pigeonite, olivine, high-Ca pyroxene (augite), low-Ca pyroxene, and numerous sulfide-metal globules interstitial to silicates (Fig. 2f, 3a-c). Globules are often <0.5 μm and up to 40 μm across, and contain varying proportions of metal and sulfide, with sulfide typically rimming metal when the proportion of metal is high (Fig. 2f, 3a-b). Chromite sometimes occurs at the edges of globules (Fig. 3b). Interstices between silicates and sulfide-metal globules in the matrix mainly consist of a feldspathic glass (Fig. 3b-c). Glass in NWA 8709 was identified by a combination of data, including optically isotropic character, lack of crystal forms, composition, and unpublished EBSD analysis. (However, no maskelynite was clearly identified.) This glass contains some vesicles and vugs adjacent to matrix silicates and globules (Fig. 3c). Elongate silicates, which

appear to be pyroxene, cross over the void spaces to form bridges between other silicate grains (Fig. 3c).

Besides the interstitial glass in matrix, glass inclusions are abundant in matrix pigeonite (Fig. 3c). Such inclusions are <0.4 μm across, and appear to be composed of a Si-Al-Na-bearing glass as well as still smaller blebs of sulfide and metal. Glass inclusions are uncommon in other matrix phases.

The melt matrix encloses irregularly-shaped or subrounded clasts. A common clast type is composed of fine-grained olivine (A, B, C in Fig. 3a). Some clasts are composed of augite + glass mixtures that appear identical to chondrule mesostases, and which were probably derived from chondrules (Fig. 2d).

Chondrules appear dark when viewed in thin section by transmitted light, mainly caused by the presence of sulfide (and minor metal) veins or inclusions that occur within the chondrules. These features are certainly shock-related and are responsible for the "blackening" recognized for some chondrites (Heymann, 1967; Britt and Pieters, 1994). The veins cross-cut portions of chondrules or surround them (chondrule A in Fig. 1b; Fig. 2a-c), and tiny (<2 μm across) blackening inclusions occur within chondrule olivine and low-Ca pyroxene (Fig. 2a-d).

An important observation is that within chondrules, sulfide veins and blackening inclusions are almost entirely restricted to coarse phases and do not occur in the mesostasis phases of chondrules (Fig. 2a-d, 2f, 1d). Mesostasis phases include pigeonite; high-Ca pyroxene (augite), which typically forms overgrowths on low-Ca pyroxene or pigeonite; fine-grained, euhedral-subhedral olivine, which occurs as isolated crystals in glass or as overgrowths on pyroxene; fine-grained low-Ca pyroxene; and glass. The sulfide veins within coarse chondrule olivine and low-Ca pyroxene often grade into glass veins of feldspathic composition, and lead to

the mesostases of the chondrules, but do not themselves cross the mesostases (Fig. 2a-c, 2f). In chondrule A of Fig. 1b, the sulfide veins are most prominent in the core of the chondrule, where they cross-cut magnesian olivine and low-Ca pyroxene, and grade into glass veins at the periphery of the chondrule, where they are associated with ferroan low-Ca pyroxene. The sulfide blackening inclusions in olivine and low-Ca pyroxene often form trails subparallel to the sulfide veins (Fig. 2a-b).

Not all chondrules within NWA 8709 are blackened. The most conspicuous examples of this are large, pyroxene-rich cryptocrystalline chondrules that completely lack sulfide veins or blackening inclusions, but which nonetheless appear dark in transmitted light owing to fine grain size (e.g., chondrule C in Fig. 1a, chondrule A in Fig. 1c-d, and chondrule A in Fig. 2e).

Some chondrules show radial variations in texture. For example, chondrule D1 in Fig. 1b grades outward into melt matrix in places, and to a less olivine-rich area distinct from matrix in other areas (D2). Similarly, chondrule A1 in Fig. 2f grades outwards into melt matrix at A3 and into a different, fine-grained portion at A2. It is unclear whether some textural variations represent single or multiple chondrules. In Fig. 1b, for example, chondrule B1 grades into a region (B2) that lacks barred texture, which may be either a subunit of B1 or a different chondrule that was attached to B1.

Besides radial changes in texture and mineralogy, chondrules sometimes show radial variations in the compositions of their phases. In chondrule A in Fig.1b, magnesian low-Ca pyroxene grades into ferroan low-Ca pyroxene at the edges. The opposite pattern is shown by chondrule C in Fig. 2e, which has a core of more ferroan low-Ca pyroxene that grades outwards into more magnesian low-Ca pyroxene.

Feldspathic glass is common within chondrule mesostases. Vesicles are often visible in this glass, though they are not abundant (Fig. 2b-c). One chondrule is exceptional in containing a central interstitial area filled not with glass but rather entirely with plagioclase (Fig. 2d). This plagioclase occurs in an olivine microporphyry chondrule containing zoned olivine and a low-Ca pyroxene rim (a Type I chondrule). As with chondrule mesostases elsewhere, no troilite veins or blackening inclusions occur in this plagioclase, although inclusions fill olivine phenocrysts on all sides of it (Fig. 2d). The central plagioclase area leads outwards first into plagioclase veins intergrown with sulfide and metal, and then into feldspathic glass veins, which eventually connect to the melt matrix (Fig. 2d).

Although glass in the melt matrix and in chondrule mesostases is dominantly feldspathic, a Si-rich glass is inhomogeneously distributed in patches throughout NWA 8709. Such glass is present within chondrules and in the matrix and can occur near feldspathic glass in both settings (Fig. 2c, 3d). As with feldspathic glass, Si-rich glass is not cross-cut by sulfide veins, and lacks blackening inclusions.

Most (~80-90%) of the metal in NWA 8709 is replaced by terrestrial weathering products, consistent with a W3 weathering grade for the meteorite. Veins filled with terrestrial weathering products are conspicuous and cross-cut all other components (Fig. 1b-c, 2a, 2c, 2d, 2f, 3d). Such weathering products are often associated with pores (Fig. 2b).

Phase composition

Average chemical compositions of olivine and pyroxene in NWA 8709 are presented in Table 2, and representative analyses for olivine, pyroxene, glass, sulfide and metal given in Tables SM-1, SM-2, and SM-3 in an electronic annex (see Supplemental Materials). Compositions of olivine and pyroxene are shown in Figures 4 and 5.

Data are grouped according to textural setting and data type (map, point analyses), with the map data more representative (Supplemental Materials). We label coarse-grained (>30 μm across) olivine and low-Ca pyroxenes in chondrules as "primary" phases, fine-grained (<10 μm across) phases in chondrule mesostases as "secondary" phases, and those present in the melt matrix as "matrix" phases. As mentioned above, only the first of these are typically blackened, and so must have pre-dated the shock blackening event. The secondary phases, in contrast, must have formed after blackening. Matrix must have formed after the formation of the chondrules, as matrix encloses the chondrules.

The composition of olivine and pyroxene grains vary in NWA 8709 (Fig. 4, 5). For olivine, Fa contents are more variable in primary chondrule settings (range $Fa_{0\text{-}22}$, mean ±1 standard deviation $Fa_{15.3\pm3.3}$) and in secondary chondrule settings ($Fa_{13\text{-}35}$, $Fa_{26.1\pm8.0}$) than in matrix ($Fa_{15\text{-}21}$, $Fa_{17.9\pm1.3}$) (Fig. 4, 5, Table 2). Similarly, for low-Ca pyroxene ($Wo_{<5}$), Fs contents are more variable in primary ($Fs_{2\text{-}37}$, $Fs_{12.6\pm6.8}$) and secondary settings ($Fs_{6\text{-}36}$, $Fs_{21.1\pm9.9}$) than in matrix ($Fs_{4\text{-}19}$, $Fs_{13.7\pm4.2}$) (Fig. 4, 5, Table 2). Pigeonite ($Wo_{5\text{-}15}$) in matrix has a relatively well-defined composition ($Wo_{7.3\pm1.9}\,Fs_{16.0\pm1.3}$), with the chief minor element components being Al_2O_3 (average ~1.4 wt%) and Cr_2O_3 (average ~1.0 wt%) (Table 2). Augite grains in matrix and chondrules have overlapping compositions (Fig. 4), with seven analyses of matrix augite giving an average composition of $Wo_{30.0\pm2.8}\ Fs_{10.9\pm0.8}$ (Table 2). The data indicate less chemical variability of olivine and pyroxene within matrix than in chondrules.

Glass compositions in matrix and chondrule mesostases are similar. Feldspathic glasses are mostly rich in an albite component ($Ab_{83\text{-}85}\,Or_{4\text{-}8}$) although some are more potassic (~Ab_{71} Or_{23}) (Table SM-2). In contrast, rare chondrule plagioclase (Fig. 2d) is notably calcic (~Ab_{55} Or_2

An_{43}) (Table EA-2). Si-rich glasses differ from feldspathic glasses in having >95 wt% SiO_2, with <3 wt% of other oxide components (Table SM-2).

Metal and sulfide analyses suggest that most metal in NWA 8709 is martensite (e.g., Wittman et al., 2010; Niihara et al., 2011; Ruzicka et al., 2017) and that most sulfide is troilite. Within matrix globules, metal has intermediate Ni contents (Ni/(Ni+Fe) ~ 0.08-0.09 wt) and elevated P contents (~0.5-0.6 wt%) (Table SM-3). Sulfide compositions in matrix globules can approach stoichiometric troilite (Fe/S ~ 1 atomic), or have an apparent deficiency of S (Fe/S ~1.15 atomic) (Table SM-3).

Olivine deformation and shock stage

Olivine grains in NWA 8709 are significantly deformed. Optical microscopy shows that most grains have deformation equivalent (Jamsja and Ruzicka, 2010; Ruzicka et al., 2015b) to shock stage S4, but a significant number have shock stage S5, and some, mostly on the margins of chondrules, have shock stage S6 (Fig. 6). The data correspond to a weighted shock stage (Jamsja and Ruzicka, 2010; Ruzicka et al., 2015b) of S4.6 ± 0.8, and to a conventional shock stage of S5 using the criteria of Stöffler et al. (1991, 2019, cf. Stöffler et al., 2018). The S5 conventional shock stage determined here is higher than the S4 shock stage previously determined based on fewer grains (MBD, 2019) and higher for NWA 8709 than for other type 3 ordinary chondrites (Stöffler et al., 1991; Bischoff et al., 2019), although it is the same as that listed for one other known L3 melt breccia, NWA 7120 (MBD, 2019), and for the L3 chondrite Gunlock (Rubin, 1994). *NWA 8709 is thus among the most strongly shocked type 3 meteorites known.*

Elemental composition

The bulk elemental composition of NWA 8709 is given in Table 3, and Fig. 7 shows abundances normalized to CI chondrites (Orgueil) and to Mg. Refractory lithophile abundances (28 elements) of NWA 8709 display a mean and 1σ standard deviation of 0.96 ± 0.11, similar to the ~0.9 × CI-Mg-normalized refractory lithophile abundances found by Kallemeyn et al. (1989) for ordinary chondrites (Fig. 7a). CI-chondrite and Mg-normalized siderophile element abundances (10 elements) in NWA 8709 have a mean and 1σ standard deviation of 0.73 ± 0.15, similar to the L chemical group (Kallemeyn et al., 1989) (Fig. 7b). However, the most abundant siderophile elements, especially Ni and Co and to a lesser extent Fe, have normalized abundances more similar to the LL group (Fig. 7b). Moderately volatile elemental abundance patterns (Mn-Bi, 14 elements) are typical for type 3 ordinary chondrites (Kallemeyn et al., 1989) (Fig. 7b). There are chemical indications of terrestrial alteration. This includes elevated U and Ag (Fig. 7), and a Ba abundance (not shown in Fig. 7) of ~10 x CI chondrites, compared to the more typical ordinary chondrite value of ~1.5 x CI chondrite for Ba (Kallemeyn et al., 1989). Altogether, compositional patterns in NWA 8709 are consistent with those of a type 3 L (or possibly LL) chondrite find.

Oxygen isotope composition

Oxygen isotope data for NWA 8709 are shown in Table 4 and Fig. 8. Four determinations were made from aliquots of two samples, CML0109-7 (acid-treated to remove terrestrial weathering products) and CML0109-1 (untreated). All four data points have similar oxygen values and fall on the edge of the L chondrite field, slightly displaced to the low-$\delta^{17}O$, high-$\delta^{18}O$ side of this field compared to other L chondrites (Fig. 8). There is no obvious systematic difference between the acid-washed and untreated samples (Table 4), suggesting that terrestrial weathering did not strongly affect the oxygen values. This is consistent with the

conclusion that oxygen isotope compositions of chondrites tend to be weakly affected by aqueous alteration, though they can be modified by strong alteration (Bland et al., 2000). The data strongly suggest an L-group affinity for NWA 8709, corroborating the initial classification. The slight shift to low $\delta^{17}O$ and high $\delta^{18}O$ values is consistent with terrestrial weathering in a hot desert environment (Bland et al., 2000; Greenwood et al., 2012).

Physical properties

Table 5 shows physical property data for a single small sample (CML0109-5C) of NWA 8709, measured first by microtomography (μCT), and then by ideal gas pycnometry and laser scanning. Data include mass, sample volume and bulk density for both methods, and grain volume, grain density and porosity from ideal gas pycnometry and laser scanning. A portion of sample 0109-5C appears to have been lost between the two measurements, evidenced from decreases in sample mass and (apparently) in sample volume. The measured porosity and grain densities are 4.1±2.1% and 3.35±0.05 g/cm^3. This porosity is lower than the averages for H, L, and LL chondrite falls (~8-9.5%) (Macke, 2010), but terrestrial weathering tends to decrease porosity in ordinary chondrites (Consolmagno et al., 1998; Bland et al., 1998, 2006), and the value for NWA 8709 is similar to the average porosities in (weathered) finds of these chondrites (~2.8-5.8%) (Macke, 2010). Similarly, grain density in NWA 8709 is lower than in H, L and LL falls, and lower than the average for H, L, and LL finds, but resembles what is found for H, L and LL chondrite finds with high weathering degree (weathering modulus), including weathered L3 chondrites (Macke, 2010). Thus, porosity and density for NWA 8709 are not much different than one would expect for a weathered ordinary chondrite.

Chondrule sizes and shapes

Chondrule sizes and shapes in NWA 8709 were studied both with microtomography (for 3D information) and optical microscopy (2D information). A typical tomogram (2D slice in a 3D rock volume) of NWA 8709 shows metal, silicate, sulfide, and weathering products as various shades of grey, a small amount of porosity (black), and the presence of chondrules (Fig. 9). Porosity within the rock is most often associated with what could be weathering products (Fig. 9), including veinlets that appear identical to weathering veinlets obvious in thin section. Digitized chondrule models, including 3D renderings, indicate that chondrules have somewhat irregular, lumpy shapes (Fig. 10).

For 3D measurements of chondrule diameter, a mean size of 940±340 μm (normal distribution) or 890 $^{+340}/_{-240}$ μm (lognormal distribution) (N=156) is obtained (Table 6). This compares to a 2D mean of 830±380 μm (normal distribution, N=53) (Table 6). The 2D and 3D datasets are consistent with one another, especially if one considers that diameters in 2D cuts through chondrules can be no larger than the maximum diameter in 3D. In detail, the 3D data for NWA 8709 suggests a strong positive skewness in chondrule diameter D (Fig. 11). The distribution features a dearth of chondrules with $D \leq 500$ μm, a mode (or peak, D_p) of ~700 μm, dropping to 50% of the peak value (D_{p50}) by ~1100 μm, and with a maximum D ~2500 μm (Fig. 11).

These chondrule sizes are large compared to those in other ordinary chondrites, judging from Friedrich et al. (2015), who compiled 2D and 3D data. These researchers suggested lognormal chondrule diameter means for H, L and LL chondrites of ~500±100 μm, with positive skew increasing in sequence H<L<LL, resulting in slightly larger chondrules overall in this sequence. Detailed chondrule size distributions were provided for Hammond Downs (H), Bjürbole (L/LL), and various LL chondrites. For these chondrites, D_p and D_{p50} values are all

smaller than in NWA 8709. The values for Hammond Downs are D_p ~400 μm and D_{p50} ~600 μm; for Björbole D_p ~550-600 μm and D_{p50} ~900 μm; and for LL chondrites D_p ~550-600 μm and D_{p50} ~1000 μm. Only the chondrules in LL chondrites approach the sizes in NWA 8709 (D_p ~700 μm, D_{p50} ~1100 μm), with both H and L/LL chondrites having significantly smaller chondrules. In NWA 8709, weathering may be biasing the averages to larger values, as smaller chondrules are more likely to be obscured by terrestrial weathering effects than larger. However, the existence of large chondrules cannot be explained by weathering, and the overall size distribution of chondrules in NWA 8709 is more similar to what is found in LL chondrites than in L or H chondrites (Friedrich et al., 2015).

Simplifying 3D chondrule shapes as best-fit ellipsoids, the chondrules in NWA 8709 tend to be slightly prolate, oblate, or triaxial, but most are still relatively equant and fall into the spheroid field of Zingg (1935) (Fig. 12). These shapes were probably not significantly affected by weathering.

Fabrics

Microtomography data were used to assess chondrule and metal grain shape fabrics in NWA 8709. These data show that the long axes of both chondrules and metal grains tend to lie in nearly the same plane (Fig. 13). This implies a common foliation for both types of particles. Foliations are commonly observed for metal grains in more strongly-shocked chondrites and have been attributed to the somewhat ductile behavior of metal during shock compaction (Friedrich et al., 2008a, 2013, 2014). The data for NWA 8709 reveal an apparently similar behavior for chondrules in this meteorite. This agrees with shock experiments and models, which show that chondrules can be flattened by shock compaction (Nakamura et al., 2000; Davison et al., 2017). The preferred alignment of metal grains, quantified by the orientation strength factor

C (Friedrich et al., 2008a), is 0.68 in NWA 8709 (Table 5). This C value is relatively high, and similar to what is observed for highly shocked chondrites, specifically those with conventional shock stages of S4-6 or a weighted shock stage of ≥S4.0 (Friedrich et al., 2017). This agrees with the conventional and weighted shock stages for NWA 8709, S5 and S4.6±0.8, respectively.

DISCUSSION

Shock melting, deformation, compaction, and thermal history

NWA 8709 shows good evidence of having been substantially melted, deformed, and compacted during an intense but short-lived shock heating event.

Shock melting. Textures suggest that all of the matrix, and parts of the chondrules, including all of the fine-grained (mesostasis) portions between coarse chondrule phases, melted and solidified following shock. Specifically, the coarse olivine and low-Ca pyroxene ("primary" phases) in chondrules are interpreted as unmelted residues, whereas the various phases within mesostases and matrix ("secondary" and "matrix" phases) are interpreted as having solidified from shock melt. Good evidence for these inferences is provided by cross-cutting relationships of sulfide and glass veins, which suggest that the veins and blackening inclusions must have formed after coarse chondrule phases, but before or during the fine-grained mesostasis phases. The composition of pigeonite and augite in matrix and chondrule mesostases in NWA 8709 are consistent with igneous temperatures (>1200 °C) (Lindsley, 1983) and support the inference that matrix and mesostasis areas crystallized from shock melt.

Deformation. Shock deformation resulted in effects corresponding to a conventional shock stage of S5 (weighted shock stage S4.6 ± 0.8) for coarse olivine (Fig. 6). Deformation produced microcracks within coarse olivine and low-Ca pyroxene that became filled with vein-like deposits of sulfide/metal and silicate glass (feldspathic) materials. Sulfide blackening

inclusions within olivine and low-Ca pyroxene probably formed in a similar way, but within cracks that became healed. Deformation involving uniaxial compression produced the common foliation observed for both metal grains and chondrules (Fig. 13).

Compaction. Compression in NWA 8709 likely produced the closely-spaced chondrules that touch or that have conforming shapes. The moderately low porosity of NWA 8709 (4.1±2.1%) could be the result of compaction, but also could have been affected by terrestrial weathering (see below). Not all porosity was removed by compaction; vugs and vesicles associated with glass in matrix (Fig. 3c) and chondrule mesostases (Fig. 2b) are interpreted as having been filled with gas generated by vaporization during melting. Silicate crystals that bridge gaps across vugs in matrix (Fig. 3c) may be condensates.

Thermal history. Although heating must have been intense in NWA 8709, it was limited in duration, as shown by the diverse compositions of olivine and low-Ca pyroxene that require limited equilibration (Fig. 4, 5). Chemical equilibrium was more closely approached in the matrix, although even here was not complete. Furthermore, cooling must have been sufficiently fast following melting to prevent much crystallization in feldspathic and siliceous melts, which instead solidified as glass. However, plagioclase in the center of one partly melted chondrule (Fig. 2d) was able to crystallize from feldspathic melt. For metal in globules, a predominant martensite composition, and elevated P content, are consistent with rapid crystallization from a metallic melt (e.g., Ruzicka et al., 2017).

NWA 8709 as a modified L3 chondrite

We interpret the data for NWA 8709 to indicate that it is a modified L chondrite. The bulk oxygen isotope composition of NWA 8709 points strongly to the L group (Fig. 8). The bulk chemical composition of the meteorite is also consistent with L group, although Ni and Co and to

a lesser extent Fe contents are low for an L chondrite (Fig. 7). Given that these siderophile elements reside chiefly in metal, which in NWA 8709 was significantly affected by terrestrial weathering, we suggest that the low contents of Ni, Co and Fe were caused by leaching during terrestrial weathering. Open system weathering is also suggested by high abundances of Ba, U, and Ag in the meteorite, and by a possible small shift in oxygen isotope composition from a more typical L chondrite composition.

If there was open-system leaching to remove Fe, Ni, and Co from metal, the porosity that is associated with terrestrial weathering products (Fig. 1b, 9) could represent locations where material was dissolved. In this case, porosity in NWA 8709 may have been increased by terrestrial weathering, as opposed to the more typical pattern of being decreased (Consolmagno et al., 1998; Macke, 2010). However, it is also possible that weathering products could have filled cracks and pore spaces incompletely, leaving some voids within the weathering products, in a process that decreased porosity overall. Finally, another possibility is that weathering resulted both in removal and addition of porosity at different times or locations. Thus, the net effect of terrestrial weathering on porosity in NWA 8709 is uncertain.

NWA 8709 has at least two anomalies that cannot be explained easily by weathering. One is that chondrule olivine and pyroxene compositions are atypical for an ordinary chondrite, as was recognized in the original 2015 classification of NWA 8709 (MBD, 2019). Another is that chondrule sizes are large for an L chondrite (Fig. 11). As explained below, we interpret these anomalies to indicate chemical and physical modifications during melt breccia formation.

The coarse and often blackened ("primary") olivine and pyroxene grains in chondrules from NWA 8709 were the least affected by shock melting—they are likely residues (see above). However, their compositions (iron contents) do not conform to what is observed for L or other

ordinary chondrites. This is shown in Fig. 15, which compares mean and 1σ standard deviation values for Fa and Fs in coarse chondrule phases from NWA 8709 to the systematics for other ordinary chondrites. In general, the iron contents of olivine and low-Ca pyroxene in ordinary chondrites change predictably during thermal metamorphism, becoming more ferroan and more uniform (more equilibrated) as metamorphic grade increases, with different mean-1σ Fa and Fs tracks for H, L and LL chondrites (Fig. 15; Grossman, 2011). In NWA 8709, olivine and low-Ca pyroxene lie off the established metamorphic tracks (Fig. 15). Considering NWA 8709 olivine, for the given 1σ Fa value, mean Fa contents are ~10 mol% lower than for an L chondrite; alternatively, for the given mean Fa value, 1σ Fa values are ~6 mol% too low (Fig. 15). This indicates that the coarse chondrule olivine in NWA 8709 is less ferroan and/or more chemically uniform than one would expect for an L chondrite affected only by thermal metamorphism. Considering coarse low-Ca pyroxene in NWA 8709 (and emphasizing the more representative EDS map data), such pyroxene is also less ferroan and/or (slightly) more chemically uniform than one would expect for an L chondrite affected by only thermal metamorphism (Fig. 15).

We suggest that *the data for coarse chondrule olivine and low-Ca pyroxene in NWA 8709 can be explained if both minerals experienced FeO-reduction, together with some chemical homogenization (more for olivine) caused by partial equilibration during the high temperatures accompanying melting.* Reactions such as the following could have occurred to decrease the iron contents of olivine and pyroxene:

Fe_2SiO_4	+	S_2	→	2FeS	+	SiO_2	+	O_2	[1]
fayalite in olivine		gas		sulfide		silica melt		gas	
$FeSiO_3$	+	½ S_2	→	FeS	+	SiO_2	+	O_2	[2]
ferrosilite in pyroxene		gas		sulfide		silica melt		gas	

Fe_2SiO_4	→	2Fe	+	SiO_2	+	O_2	[3]
fayalite in olivine		metal		silica melt		gas	
$FeSiO_3$	→	Fe	+	SiO_2	+	O_2	[4]
ferrosilite in pyroxene		metal		silica melt		gas	

In reactions [1] and [2], it is assumed that some vaporization of S occurs during the melting of troilite in the L chondrite precursor, and that the S-bearing gas reacts with iron-bearing silicates to produce 1) a more magnesian silicate residue, 2) a sulfide that is deposited within these residues (to create blackening), and 3) a siliceous melt. Gooding and Muenow (1977) showed that during experimental heating of ordinary chondrites, S_2 is one of the main gases produced. Impact-induced S vaporization was previously inferred for the Smyer H melt breccia (Rubin, 2002), the PAT 91505 impact melt (Benedix et al., 2008), the Chelyabinsk melt breccia (Andronikov et al., 2015), and the eucrite NWA 2339 (Zhang et al., 2013). In reactions [3] and [4], magnesian silicate residue, siliceous melt, and metal are produced directly by FeO reduction.

Other data for NWA 8709 may be consistent with these reactions. Reverse Fe-Mg zoning in pyroxene from some chondrules (more magnesian grain rims in Fig. 2c, more magnesian chondrule edges for object C in Fig. 2e) suggests FeO-reduction, as such zoning is opposite to what should be produced by igneous processes accompanying chondrule crystallization or the partial melting of chondrules. Evidence for FeO-reduction in olivine from NWA 8709 is less obvious, possibly owing to enhanced Fe-Mg diffusion in olivine compared to pyroxene (Chakraborty, 1997; Ganguly and Tazzoli, 1994), which would have tended to obliterate evidence for reverse zoning if some homogenization occurred. Abundant blackening, mainly by sulfide but also by metal, could be consistent with reactions [1] through [4], although most metal

in NWA 8709 appears to be Ni-bearing martensite and does not have the Ni-free composition one would expect based on reactions [3] and [4]. Si-rich glass is common in NWA 8709 and can be explained as solidified silica melt produced as a by-product of the FeO-reduction reactions above, although other reactions also can produce such glass (see below). For reactions [1] through [4], oxygen gas is evolved, and such gas could have filled vesicles and vugs prior to escaping (Fig. 2b, Fig. 3c).

We suggest that *the large sizes of chondrules in NWA 8709 can be explained by physical modifications of pre-existing chondrules*. One mechanism for creating apparently larger chondrules during melt-breccia formation is attachment and accretion. Another is the incorporation of melt into chondrules, allowing them to inflate.

There is petrographic evidence for the clumping and attachment of chondrules, and for textural variations at chondrule edges that could represent accretion to pre-existing chondrules. For example, in Fig. 2e, three separate chondrules (A, B, C) have clearly become attached to make a larger unit. In Fig. 1b, objects B1 and B2 could represent two separate chondrules that became attached to form an object twice as big, and chondrule C has clearly become molded against B1 to make this object still larger. In Fig. 1c-d, four separate chondrules (A, B, C, D) are attached to form a matrix-free cluster ~1.5 mm across. In Fig. 2f, the chondrule core A1 transitions into a matrix-like area at A3 but has a marginal zone at A2 that is distinct from matrix. Zone A2 resembles chondrule mesostases and could represent material that melted, solidified, and accreted onto A1. A similar process may have affected object D1 in Fig. 1b, which in places transitions into melt matrix, and which elsewhere (D2) transitions into a marginal, mesostasis-like area distinct from matrix. Chondrule attachment and accretion would tend to make apparently lumpy chondrules, as observed (Fig. 10). This process of chondrule

attachment during shock is similar to what was inferred to create melded chondrules in a clast from Plainview (Rubin et al., 2005).

Melt incorporation from the surroundings is another possible way to make larger chondrules. This is analogous to the process suggested for clusters of zircon grains in impact melt rock from the terrestrial Acraman crater (Schmieder et al., 2015). Candidates for such "melt inflation" in NWA 8709 include both fine-grained olivine-rich clasts (Fig. 3a) and fine-grained pyroxene-rich chondrules (Fig. 3e). These consist of fine-grained crystallites of olivine and pyroxene with intervening likely melt-derived phases, similar in texture to the zircon clusters in Acraman (Schmieder et al., 2015). The fine-grained olivine and pyroxene objects in NWA 8709 are not blackened, implying they crystallized from melt.

The pyroxene-rich cryptocrystalline chondrules are representative of some of the largest chondrules in NWA 8709, although some large chondrules are microporphyries. They could have been melted entirely during breccia formation, producing secondary or "ghost" chondrules similar to that inferred for the Ramsdorf chondrite melt rock (Yamaguchi et al. (1999). Complete melting of these chondrules would have been enhanced if the original chondrules were fine-grained and pyroxene-rich. An initial fine grain size would have a larger grain surface area and permit easier conduction with superheated melts, allowing more complete melting; and a pyroxene-rich composition would have a comparatively low melting temperature (relative to an olivine-rich chondrule), making it easier to melt. The distinctive sharp edges of the pyroxene-rich cryptocrystalline chondrules in NWA 8709 was noted also for Ramsdorf, where it was attributed to high melt viscosity of a pyroxene-rich melt (Yamaguchi et al., 1999). However, if these chondrules were completely melted and superheated, they could have been able to assimilate surrounding material to make a larger volume of melt, growing in size. Although the

three cryptocrystalline chondrules highlighted in Figures 1a (object C), 1c (object A) and 2e (object A) show no radial variations in texture, others show an increasing proportion of olivine towards their edges. The latter objects could be reflecting the assimilation of olivine-rich material into otherwise pyroxene-normative melts.

Despite significant chemical and physical modifications, we identify the protolith of NWA 8709 as being a type 3 chondrite. Chemical variations in olivine and pyroxene are largest in the least melted parts of chondrules, and least in the matrix which was most thoroughly melted, suggesting that the chemical variations were present prior to melting. This would indicate a type 3 chondrite. Further, the abundances of volatile elements in the meteorite are consistent with a type 3 chondrite, and the large differences in grain size between matrix and chondrules is most consistent with a type 3 precursor.

Conditions needed to create melt breccias

The most significant features of NWA 8709 are the melt breccia character and igneous texture of the matrix. Even strongly shocked analogues of NWA 8709, which have similar shock stages, metal foliations, and porosities, such as Morrow County (L6 S5) and Tenham (L6 S5) (Friedrich et al., 2017), lack evidence for being melt breccias. There must have been a key difference in the shock conditions between NWA 8709 and these other strongly shocked chondrites to produce an igneous matrix only in NWA 8709.

We infer that the key difference in these shocked chondrites was porosity of the immediate precursor. Target porosity is known to be an important variable during impacts (Kieffer, 1971, 1975; Davison et al., 2010, 2012; Kowitz et al., 2013; Flynn et al., 1999, 2015). Bland et al. (2014) and Davison et al. (2016, 2017) have shown by numerical modeling that shock heating effects will be strongly concentrated in the porous matrices of chondritic

agglomerates. For a sufficiently porous matrix and sufficient collisional velocity, this can result in preferential melting of matrix.

For example, Bland et al. (2014) modelled impacts occurring in a simplified ordinary chondrite-like mixture of non-porous chondrules and porous matrix, with 23% original porosity overall. For impact speeds of 2-3 km/s, the models showed 94-100% melting of the matrix. For a 3 km/s impact with complete matrix melting, the model results entailed bulk shock pressures of ~20 GPa, a peak shock pressure in chondrules of ~25 GPa, a final bulk porosity of 2%, and a peak temperature in matrix and chondrules of ~3900 K and ~750 K, respectively. A 25 GPa peak pressure for chondrules corresponds to a conventional shock stage of S4 (Stöffler et al., 1991), which is the most frequent value determined for NWA 8709 olivine (Fig. 6). In addition, the modelled final bulk porosity of 2% is not very different from the porosity determined for NWA 8709, 4.1±2.1%, which was more-or-less affected by terrestrial weathering. The final model matrix temperature is so high that some of the constituents in the matrix of a chondrite undergoing such shock conditions should have been vaporized. This is consistent with the observation of vugs and vesicles associated with glass in NWA 8709, implying that gas was generated by vaporization during melting. For impact velocities of ≥2 km/s, chondrule flattening can occur (Davison et al., 2016), as was the case for NWA 8709 to form a foliation (Fig. 13a). Thus, *numerical modeling results broadly agree with observations, and suggest that a ~3 km/s impact event affecting an L3 chondrite precursor with ~23% initial porosity can account for the characteristics of NWA 8709.*

Given the results reported by Bland et al. (2014) and Davison et al. (2016, 2017), the combination of initial porosity and impact velocity needs to be sufficiently high to result in matrix melting. In principle, plausible conditions to create NWA 8709 and other melt breccias

could be a combination of higher impact velocity (>3 km/s) and lower porosity (<23%), or lower impact velocity (<3 km/s) and higher porosity (>23%). However, models suggest there is an apparently lower limit of impact velocity of ~2 km/s to create substantially melted matrix, even with much higher target porosities (Bland et al., 2014; Davison et al., 2016).

Conversely, if porosity and impact velocity were both too high, a melt rock as opposed to melt breccia would have been produced. Davison et al. (2010) have estimated that liquidus temperatures would be reached for impact velocities of ~6 km/s to ~4 km/s with porosities of 20% to 50%, respectively. Melt rock formation could be promoted also by the formation of thicker or deeper melt deposits (in melt veins, dikes, breccia lenses) (e.g., Wittman et al., 2010; Schmieder et al., 2016) that would cool more slowly and which would help digest clasts, conditions presumably achieved with a higher impact velocity and a more porous target (Davison et al., 2012). Melt rocks might be easier to generate also by increasing shear stress (Niihara et al., 2011), which could help break up clasts into more easily melted smaller pieces.

If porosity and impact velocity were primary controls, it follows that the rarity of ordinary chondrite melt breccias in our collection must indicate either that most ordinary chondrites were not especially porous prior to the last significant impact, or that impact velocities in the last significant impact were always insufficiently high. The latter cannot be the generally correct explanation for chondrites, as there are many highly shocked chondrites that are not melt breccias but which require elevated collision velocities (Stöffler et al., 1991; Bischoff et al., 2019). There are many shock stage S4 L chondrites (Stöffler et al., 1991; Bischoff et al., 2019), for example, and these must have been much less porous than NWA 8709 prior to the shock that established their final S4 character, for otherwise they would be melt breccias.

Thus, we surmise that *the overall rarity of ordinary chondrite melt breccias indicates that most ordinary chondrites prior to their last shock event (what we term "immediate precursors") were low in porosity (<23% and possibly much less).* The typical porosity for ordinary chondrite falls is ~8-9.5% (Macke 2010), which may have been too low to allow melt breccias to form in most shock events. Some especially porous (~10-20%) ordinary chondrites are known, but they are weakly shocked (shock stages S1 or S2) (Przylibski et al., 2003; Sasso et al., 2009; Macke, 2010; Friedrich et al., 2017; Krzesińska and Almeida, 2019), and evidently experienced low-velocity collisions. A similar situation could pertain to the generally more porous carbonaceous chondrites (average porosity ~0-25% for various groups, 35% for CI; Macke, 2010), which mostly have S1 shock stages (Scott et al., 1992).

A larger question is how the low porosities of immediate precursors were established. Theoretical and experimental results of dust growth and accretion in the nebula suggest that initial collision velocities would have been very low (Blum and Wurm, 2000; Cuzzi et al., 2008; Guttler et al., 2010; Beitz et al., 2013), implying very high porosities (~90-95%) for aggregates (Beitz et al., 2013). Furthermore, data for a fine-grained chondrule rim in the Allende (CV3) chondrite was used to infer an initial porosity of ~70-80% for matrix-like materials (Bland et al., 2011). All of this suggests that proto-chondrites would have been porous. Through weak impact events, these could have been converted into the low-porosity chondrites now observed (Hirata et al., 1998; Beitz et al., 2013; Bland et al., 2014). Thus, *the data for NWA 8709 support the inference that the immediate precursors to most ordinary chondrites must have become compacted by early, low-velocity collisions.* The immediate precursor to NWA 8709, in contrast, would have been more porous and less affected by such collisions, prior to the event that created the melt breccia.

NWA 8709: primordial or processed, and constraints for the accretion era

As discussed above, the immediate precursor to NWA 8709 must have been relatively porous (~23%) prior to the shock event that created the melt breccia. Either this porous precursor formed as a "primordial porous aggregate", or proto-chondrite, as hypothesized for the early stages of chondrite formation (Bland et al., 2014), or it became porous by the later processing of chondritic material. The type 3 character of NWA 8709, which implies that it escaped deep burial and metamorphic heating in an asteroidal body, is consistent with the idea that the precursor to NWA 8709 was in some sense a primordial aggregate, although it was not a highly porous (e.g. 70-80%) first-generation proto-chondrite (Bland et al., 2011, 2014).

The NWA 8709 immediate precursor may have been more analogous to porous (~10-20%) type 5 ordinary chondrites known from different groups (H, L, LL) (Przylibski et al., 2003; Sasso et al., 2009). These type 5 chondrites experienced a higher degree of thermal metamorphism than NWA 8709 and have low (S1, S2) shock stages (Sasso et al., 2009; Friedrich et al., 2008b). They may have formed by weak shock compaction (Sasso et al., 2009; Friedrich et al., 2008b), experiencing fewer or weaker shock events than other chondrites and preserving more of their original porosity despite burial and metamorphic heating. The NWA 8709 precursor may have been similar, except somewhat more porous and less metamorphosed, maintaining its type 3 character.

Alternatively, it has been suggested that porosity in one of the porous type 5s (Baszkówka) was created by impact vaporization and rapid re-accretion of a hot, gas-bearing mixture, with post-accretional annealing obliterating much evidence for shock and lowering the shock stage to S1 (Krzesińska and Almeida, 2019). If this model is correct, it raises the question

of whether the precursor to NWA 8709 could have been processed in this way. Although impact vaporization cannot be ruled out for having introduced porosity in the NWA 8709 precursor, it probably was not followed by the annealing hypothesized to have occurred for Baszkówka to establish an S1 shock stage (Krzesińska and Almeida, 2019). Such annealing would tend to destroy the type 3 character of a chondrite, inconsistent with the type 3 precursor inferred for NWA 8709 (see above).

Regardless of whether the NWA 8709 immediate precursor was primordial or processed, it provides constraints on the collisional environments involved in producing most type 3 ordinary chondrites. Unlike these chondrites, NWA 8709 evidently experienced a moderately strong impact while it was still relatively porous (~23%). Instead, most type 3 chondrites must have become less porous as a result of weaker shocks, prior to the last stronger shocks experienced by some. *This implies a relatively "quiet" dynamical environment in the accretion era for most ordinary chondrites*.

Comparison to MIL 07273: how standard is the melt breccia "recipe"?

An instructive comparison of NWA 8709 can be made to Miller Range (MIL) 07273, an anomalous H5 melt breccia that was studied in detail (Ruzicka et al., 2017). There are similarities and dissimilarities between NWA 8709 and MIL 07273, which suggest common processing mechanisms as well as some variations.

Similarities include a complete melting of matrix, partial melting of chondrules, extensive mobilization of troilite into veins, and common deformation of chondrule olivine to an S4 level (MIL 07273 has a weighted shock stage of S4.0±0.5) (Ruzicka et al., 2017). The data for both meteorites suggest preferential melting of matrix caused by strong shock of an originally

porous precursor (H5 in the case of MIL 07273, Ruzicka et al., 2017; L3 in the case of NWA 8709).

Porosity and metal fabric differ somewhat between the two meteorites (Fig. 14). In MIL 07273, porosity is very low (0.6±0.2%), and the metal orientation strength factor has a moderately low value (C=0.25) (Ruzicka et al., 2017). The low porosity is not the result of weathering, given the minor metal replacement seen in MIL 07273 (Ruzicka et al., 2017), and could be more representative of strong compaction than the higher, possibly weathering-affected value (4.1±2.1%) in NWA 8709.

On the other hand, we suggest that the higher C value (0.68) in NWA 8709 compared to MIL 07273 is more representative of strong shock. The moderately low C value in MIL 07273 is not as high as one would expect based on the shock stage (Friedrich et al., 2017), and may be related to the particular shock conditions experienced by the metal. It was inferred that coarse metal in MIL 07273 was partly liquefied by shock and cooled rapidly afterwards, and formed into distinctive, aligned cone shapes as a result of deformation in an overarching stress field (Ruzicka et al., 2017). In MIL 07273, a cooling rate of ~1-2 °C/s at >1300 °C was inferred from the properties of metal (Ruzicka et al., 2017). The conditions in MIL 07273, especially partial liquefaction of metal and rapid (but perhaps not too rapid) post-shock cooling, may have enabled metal to solidify in shapes that did not align as much in their long axes as typical for shocked chondrites.

The matrix regions of the two melt breccias, although grossly similar in fine grain size and apparent igneous texture, show intriguing differences. Chief among these is that MIL 07273 has a strong depletion of a feldspar component, a higher proportion of pyroxene to olivine, and an omphacitic (Na-Al-rich) composition of pigeonite. These features were attributed to reactions

occurring at high pressure and temperature during shock (Ruzicka et al., 2017). The depletion of feldspar was attributed to the breakdown of albitic feldspar and conversion to a jadeite component, according to the reaction:

$NaAlSi_3O_8$	→	$NaAlSi_2O_6$	+	SiO_2	[5]
albite melt		jadeite in pyroxene		silica melt	

The pyroxene-rich composition of matrix (high pyroxene/olivine ratio) was attributed to the conversion of olivine to pyroxene:

$(Mg,Fe)_2SiO_4$	+	SiO_2	→	$(Mg,Fe)_2Si_2O_6$	[6]
olivine		silica melt		pyroxene	

In MIL 07273, the operation of reactions [5] and [6] together do not result in any excess silica, consistent with the lack of a silica phase in MIL 07273 (Ruzicka et al., 2017). In NWA 8709, there is no evidence for reaction [6], but possible evidence for reaction [5]. Although pigeonite in NWA 8709 is not itself rich in Na and Al (or jadeite component), it does contain numerous glass inclusions (Fig. 3b-c), which contain these elements. This suggests that a pigeonite precursor in NWA 8709 once could have been omphacitic, but that it decomposed upon pressure release and cooling to form pigeonite containing Na-Al-bearing inclusions that solidified as glass. Reaction [5] in MIL 07273 was inferred to have occurred at pressures >3 GPa (Ruzicka et al., 2017). Peak pressures in NWA 8709 likely exceeded 3 GPa as well (e.g., possibly ~25 GPa according to the frequent S4 shock level observed for olivine and as suggested by numerical models—see above), but may have been followed by slower cooling than in MIL 07273, allowing more back-reaction to a lower-pressure mineralogy. Reaction [5] results in excess silica, providing another way besides reactions [1] through [4] to produce the Si-rich glass found in NWA 8709. The lack of evidence for reaction [6] in NWA 8709 could indicate either that it never occurred (peak

pressures may have been insufficiently high), or that it did occur, but was followed upon cooling and pressure release by back-reaction that was more extensive compared to that in MIL 07273. *Possibly NWA 8709 originated in a larger volume of heated rock (or at greater depth) compared to MIL 07273, causing it to cool more slowly following shock, and erasing more evidence of high-pressure formation, while still cooling sufficiently fast to preserve glass and chemical variability.* A larger volume of heated rock for NWA 8709 could have resulted from a larger impact event or a different setting within or below an impact crater than that which produced MIL 07273.

CONCLUSION

- NWA 8709 is an L3 melt breccia that is among the most strongly shocked type 3 chondrites known.
- The matrix completely melted during shock reheating. Pigeonite is a prominent matrix phase and is notable for containing melt inclusions composed of feldspathic glass and metal-sulfide, which may have been produced upon decompression.
- Chondrules were partly melted. The textural occurrence and cross-cutting relationships of sulfide veins and blackening inclusions strongly imply that coarse chondrule olivine and low-Ca pyroxene grains are residual, unmelted phases, whereas the mesostases of microporphyritic chondrules were completed melted during shock.
- Unmelted phases experienced FeO-reduction and partial homogenization. Reduction possibly occurred by reaction of olivine and low-Ca pyroxene with an S-bearing gas that was produced by vaporization.
- Chondrules and metal grains became foliated by uniaxial compression during shock.

- During compression, chondrules and fragments became attached to form larger clumps. Chondrules may have been enlarged by incorporating melt from their surroundings.
- An L3 protolith for NWA 8709 is inferred on basis of oxygen isotope composition, elemental composition, diverse mineral chemistry, and overall texture.
- The melt breccia character on NWA 8709 is attributed to strong shock affecting a porous precursor. Data-model comparisons suggest that a precursor with 23% porosity that was impacted by a 3 km/s projectile could have produced the meteorite.
- The rarity of ordinary chondrite melt breccias implies that most ordinary chondrite immediate precursors were lower in porosity than the NWA 8709 precursor.
- Altogether, the data imply a predominantly "quiet" dynamical (collisional) environment to form ordinary chondrite precursors, with compaction occurring through what was probably a succession of weak shock events. This was punctuated by occasional high-velocity collisions. The combination of especially weak early compaction, followed by a single strong impact event, produced NWA 8709.

Acknowledgments
AMR, MLH, and RNP gratefully acknowledge funding for this study that was provided partly by public donations to the Cascadia Meteorite Laboratory at Portland State University, and partly by NASA (Emerging Worlds, Grant #80NSSC19K0517). Portions of this work were performed at GeoSoilEnviroCARS (Sector 13), Advanced Photon Source (APS), Argonne National Laboratory. GeoSoilEnviroCARS is supported by the National Science Foundation - Earth Sciences (EAR-1128799) and Department of Energy- GeoSciences (DE-FG02-94ER14466). This research used resources of the Advanced Photon Source, a U.S. Department of Energy (DOE) Office of Science User Facility operated for the DOE Office of Science by Argonne National Laboratory under Contract No. DE-AC02-06CH11357. JMF would like to thank the Camille and Henry Dreyfus Special Grant Program in the Chemical Sciences for providing vital material support. JWS received support from the Henry Luce Foundation via a Clare Boothe Luce Program summer research fellowship. Thoughtful reviews by Martin Schmieder, Alan Rubin, and Cyrena Goodrich are appreciated and helped make this a better paper. The authors have no conflict of interest to declare.

REFERENCES

Agee C. B., Wilson N. V., McCubbin F. M., Ziegler K., Polyak V. J., Sharp, Z. D., Asmerom Y., Nunn M.H., Shaheen R., Thiemens M.H., and Steele A. 2013. Unique meteorite from early Amazonian Mars: Water-rich basaltic breccia Northwest Africa 7034. *Science* 339: 780-785.

Andronikov A.V., Andronikova I.E. and Hill D.H. 2015. Impact history of the Chelyabinsk meteorite: Electron microprobe and LA-ICP-MS study of sulfides and metals. *Planetary and Space Science* 118: 54-78.

Beitz E., Güttler C., Nakamura A.M., Tsuchiyama A. and Blum J. 2013. Experiments on the consolidation of chondrites and the formation of dense rims around chondrules. *Icarus* 225(1): 558-569.

Benedix G.K., Ketcham R.A., Wilson L., McCoy T.J., Bogard D.D., Garrison D.H., Herzog G.F., Xue S., Klein J. and Middleton R. 2008. The formation and chronology of the PAT 91501 impact-melt L chondrite with vesicle–metal–sulfide assemblages. *Geochimica et Cosmochimica Acta* 72(9): 2417-2428.

Bischoff A., Schleiting M. and Patzek M. 2019. Shock stage distribution of 2280 ordinary chondrites—Can bulk chondrites with a shock stage of S6 exist as individual rocks? Meteoritics & Planetary Science 54: 2189-2202.

Bland P.A., Sexton A.S., Jull A.T., Bevan A.W.R., Berry F.J., Thornley D.M., Astin T.R., Britt D.T. and Pillinger C.T., 1998. Climate and rock weathering: A study of terrestrial age dated ordinary chondritic meteorites from hot desert regions. *Geochimica et Cosmochimica Acta*, 62(18): 3169-3184.

Bland P.A., Lee M.R., Sexton A.S., Franchi I.A., Fallick A.E.T., Miller M.F., Cadogan J.M., Berry F.J. and Pillinger C.T., 2000. Aqueous alteration without a pronounced oxygen-isotopic shift: Implications for the asteroidal processing of chondritic materials. Meteoritics & Planetary Science 35(6): 1387-1395.

Bland P.A., Zolensky M.E., Benedix G.K. and Sephton M.A., 2006. Weathering of chondritic meteorites. In *Meteorites and the Early Solar System II* (eds. D.S. Lauretta and H.Y. McSween, Jr.), pp. 853-867. University of Arizona Press: Tucson.

Bland P.A., Howard L.E., Prior D.J., Wheeler J., Hough R.M. and Dyl K.A. 2011. Earliest rock fabric formed in the Solar System preserved in a chondrule rim. *Nature Geoscience* 4(4), 244.

Bland P.A., Collins G.S., Davison T.M., Abreu N.M., Ciesla F.J., Muxworthy A.R. and Moore J. 2014. Pressure–temperature evolution of primordial solar system solids during impact-induced compaction. *Nature communications* 5: 5451-5463.

Blum J. and Wurm G., 2000. Experiments on sticking, restructuring, and fragmentation of preplanetary dust aggregates. *Icarus* 143(1): 138-146.

Brearley A.J. and Jones R.H. 1998. Chondritic meteorites. In *Planetary Materials* (ed. J.J. Papike), Reviews in Mineralogy, Vol. 36, pp. 3-1 to 3-398. Washington, D.C.: Mineralogical Society of America.

Britt D.T. and Pieters C.M. 1994. Darkening in black and gas-rich ordinary chondrites: The spectral effects of opaque morphology and distribution. *Geochimica et Cosmochimica Acta*, 58(18): 3905-3919.

Cardona A., Saalfeld S., Schindelin J., Arganda-Carreras I., Preibisch S., Longair M., Tomancak P., Hartenstein V. and Douglas R.J. 2012. TrakEM2 software for neural circuit reconstruction. PLoS ONE 7(6): e38011.

Chakraborty S. 1997. Rates and mechanisms of Fe-Mg interdiffusion in olivine at 980° –1300°C. *Journal of Geophysical Research* 102(B6): 12,317-12,331, June 10th, 1997.

Clayton R.N., Mayeda T.K., Goswami J.N. and Olsen E.J. 1991. Oxygen isotope studies of ordinary chondrites. *Geochimica et Cosmochimica Acta* 55(8): 2317-2337.

Consolmagno G.J., Britt D.T. and Stoll, C.P. 1998. The porosities of ordinary chondrites: Models and interpretation. *Meteoritics & Planetary Science* 33(6): 1221-1229.

Cuzzi J.N., Hogan R.C. and Shariff K. 2008. Toward planetesimals: Dense chondrule clumps in the protoplanetary nebula. *The Astrophysical Journal* 687(2): 1432-1447.

Davison T.M., Collins G.S. and Ciesla F.J., 2010. Numerical modelling of heating in porous planetesimal collisions. *Icarus* 208(1): 468-481.

Davison T.M., Ciesla F.J. and Collins G.S., 2012. Post-impact thermal evolution of porous planetesimals. *Geochimica et Cosmochimica Acta* 95: 252-269.

Davison T.M., Collins G.S. and Bland P.A. 2016. Mesoscale modeling of impact compaction of primitive solar system solids. *The Astrophysical Journal* 821(1): 68-86.

Davison T.M., Derrick J.G., Collins G.S., Bland P.A., Rutherford M.E., Chapman D.J. and Eakins D.E. 2017. Impact-induced compaction of primitive solar system solids: The need for mesoscale modelling and experiments. *Procedia engineering* 204:.405-412.

Ebel D.S. and Rivers M.L. 2007. Meteorite 3-dimensional synchrotron microtomography: methods and applications. *Meteoritics & Planetary Science* 42: 1627–1646.

Flynn G.J., Moore L.B. and Klöck W. 1999. Density and porosity of stone meteorites: Implications for the density, porosity, cratering, and collisional disruption of asteroids. *Icarus* 142(1): 97-105.

Flynn G.J., Durda D.D., Patmore E.B., Clayton A.N., Jack S.J., Lipman M.D. and Strait M.M. 2015. Hypervelocity cratering and disruption of porous pumice targets: Implications for crater production, catastrophic disruption, and momentum transfer on porous asteroids. *Planetary and Space Science* 107: 64-76.

Friedrich J.M. 2014. A classroom-based distributed workflow initiative for the early involvement of undergraduate students in scientific research. *Journal of Science Education and Technology* 23: 59-66. doi: 10.1007/s10956-013-9450-z

Friedrich J.M., Wang M.-S. and Lipschutz M.E. 2003. Chemical studies of L chondrites. V: Compositional patterns for 49 trace elements in 14 L4-6 and 7 LL4-6 Falls. *Geochimica et Cosmochimica Acta* 67**:** 2467-2479.

Friedrich J.M., Wignarajah D. P., Chaudhary S., Rivers M.L., Nehru C.E. and Ebel D.S. 2008a. Three-dimensional petrography of metal phases in equilibrated L chondrites–Effects of shock loading and dynamic compaction. *Earth and Planetary Science Letters* 275: 172-180. doi:10.1016/j.epsl.2008.08.024

Friedrich J.M., Macke R.J., Wignarajah D.P., Rivers M.L., Britt D.T. and Ebel D.S., 2008b. Pore size distribution in an uncompacted equilibrated ordinary chondrite. *Planetary and Space Science* 56(7): 895-900.

Friedrich J.M., Ruzicka A., Rivers M.L., Ebel D.S., Thostenson J.O., and Rudolph R.A. 2013. Metal veins in the Kernouvé (H6 S1) chondrite: Evidence for pre- or syn-metamorphic shear deformation. *Geochimica et Cosmochimica Acta* 116: 71-83. doi: 10.1016/j.gca.2013.01.009

Friedrich J.M., Weisberg M.K., and Rivers M.L. 2014. Multiple impact events recorded in the NWA 7298 H chondrite breccia and the dynamical evolution of an ordinary chondrite asteroid. *Earth and Planetary Science Letters* 394: 13-19. doi: 10.1016/j.epsl.2014.03.016

Friedrich J.M., Weisberg M.K., Ebel D.S., Biltz A.E., Corbett B.M., Iotzov I.V., Khan W.S., Wolman M.D. 2015. Chondrule size and related physical properties: a compilation and evaluation of current data across all meteorite groups. *Chemie der Erde – Geochemistry* 75 (4): 419-443. doi: 10.1016/j.chemer.2014.08.003

Friedrich J.M, Ruzicka A., Macke R.J., Thostenson J.O., Rudolph R.A. Rivers M.L. and Ebel D.S. 2017. Relationships among physical properties as indicators of high temperature deformation or post-shock thermal annealing in ordinary chondrites. *Geochimica et Cosmochimica Acta* 203: 157-174.

Ganguly J. and Tazzoli V. 1994. Fe^{2+}-Mg interdiffusion in orthopyroxene: Retrieval from the data on intra crystalline exchange reaction. *American Mineralogist* 79: 930-937.

Gooding J.L. and Muenow D.W. 1977. Experimental vaporization of the Holbrook chondrite. *Meteoritics* 12(4): 401-408

Greenwood R., Franchi I., Gibson J. and Benedix G. 2012. Oxygen isotope variation in primitive achondrites: The influence of primordial, asteroidal and terrestrial processes. *Geochimica et Cosmochima Acta* 94: 146–163.

Grossman J. 2011. Classification of ordinary chondrites based on mean and standard deviation of Fa and Fs contents of mafic silicates. Sequel to "White paper report for the Nomenclature Committee on the composition of olivine and pyroxene in equilibrated ordinary chondrites." https://www.lpi.usra.edu/meteor/docs/whitepaper-supp.pdf

Grossman J. and Rubin A.E. 2006. White paper report for the Nomenclature Committee on the composition of olivine and pyroxene in equilibrated ordinary chondrites. https://www.lpi.usra.edu/meteor/docs/whitepaper.pdf

Güttler C., Blum J., Zsom A., Ormel C.W. and Dullemond C.P. 2010. The outcome of protoplanetary dust growth: pebbles, boulders, or planetesimals?-I. Mapping the zoo of laboratory collision experiments. *Astronomy & Astrophysics* 513: A56. DOI: 10.1051/0004-6361/200912852.

Heymann D. 1967. On the origin of hypersthene chondrites: Ages and shock effects of black chondrites. *Icarus* 6(1-3): 189-221.

Hirata N., Kurita K. and Sekine T. 1998. Experimental shock lithification of porous powder mixture. Lunar and Planetary Science XXIX, Abstract #1345.

Jamsja N. and Ruzicka A. 2010. Shock and thermal history of Northwest Africa 4859, an annealed impact-melt breccia of LL chondrite parentage containing unusual igneous features and pentlandite. *Meteoritics & Planetary Science* 45(5): 828-849.

Kallemeyn G.W., Rubin A E., Wang D. and Wasson J.T. 1989. Ordinary chondrites – Bulk compositions, classification, lithophile-element fractionations, and composition-petrographic type relationships. *Geochimica et Cosmochimica Acta* 53: 2747-2767.

Ketcham R.A. 2005. Computational methods for quantitative analysis of three-dimensional features in geological specimens. *Geosphere* 1: 32–41.

Kieffer S.W. 1971. Shock metamorphism of the Coconino sandstone at Meteor Crater, Arizona. *Journal of Geophysical Research* 76(23): 5449-5473.

Kieffer S.W., 1975. From regolith to rock by shock. *The Moon* 13(1-3): 301-320.

Krzesińska A.M. and Almeida N.V. 2019. Evidence of shock-induced vaporization of matrix to form porosity in Baszkówka, a porous L5 chondrite. *Meteoritics & Planetary Science* 54(1): 54-71.

Lindsley D.H. 1983. Pyroxene thermometry. *American Mineralogist* 68(5-6): 477-493.

Macke R.J., 2010. Survey of Meteorite Physical Properties Density, Porosity and Magnetic Susceptibility. Doctoral Dissertation (Open Access), University of Central Florida, 311 pp.

MBD 2019. Meteoritical Bulletin Database. https://www.lpi.usra.edu/meteor/

Miller M.F., Franchi I.A., Sexton A.S. and Pillinger C.T. 1999. High precision $\delta^{17}O$ isotope measurements of oxygen from silicates and other oxides: method and applications. *Rapid Communications in Mass Spectrometry* 13(13): 1211–1217.

Nakamura T., Tomeoka K., Takaoka N., Sekine T. and Takeda H. 2000. Impact-induced textural changes of CV carbonaceous chondrites: experimental reproduction. *Icarus* 146(1): 289-300.

Niihara T., Imae N., Misawa K. and Kojima H. 2011. Petrology and mineralogy of the shock-melted H chondrites Yamato–791088 and LaPaz Ice Field 02240. *Polar Science* 4(4): 558-573.

Przylibski T.A., Pilski A.S., Zagożdżon P.P. and Kryza R. 2003. Petrology of the Baszkówka L5 chondrite: A record of surface-forming processes on the parent body. Meteoritics & Planetary Science 38(6): 927-937.

Rubin A.E. 1994. Metallic copper in ordinary chondrites. *Meteoritics* 29(1): 93-98.

Rubin A.E. 2002. Smyer H-chondrite impact-melt breccia and evidence for sulfur vaporization. *Geochimica et Cosmochimica Acta* 66(4): 699-711.

Rubin A.E., Trigo-Rodriguez J.M., Kunihiro T., Kallemeyn G.W. and Wasson J.T. 2005. Carbon-rich chondritic clast PV1 from the Plainview H-chondrite regolith breccia: Formation from H3 chondrite material by possible cometary impact. *Geochimica et Cosmochimica Acta* 69(13): 3419-3430.

Ruzicka A.M., Hutson M., Friedrich J.M., Bland P.A. and Pugh R. 2015a. Northwest Africa 8709: A rare but revealing type 3 ordinary chondrite melt breccia. *Meteoritics & Planetary Science*, Abstract #5348.

Ruzicka A., Hugo R. and Hutson M. 2015b. Deformation and thermal histories of ordinary chondrites: Evidence for post-deformation annealing and syn-metamorphic shock. *Geochimica et Cosmochimica Acta* 163: 219-233.

Ruzicka A., Hutson M., Friedrich J.M., Rivers M.L., Weisberg M.K., Ebel D.S., Ziegler K., Rumble D. and Dolan A.A. 2017. Petrogenesis of Miller Range 07273, a new type of anomalous melt breccia: Implications for impact effects on the H chondrite asteroid. *Meteoritics & Planetary Science* 52: 1963-1990.

Sasso M.R., Macke R.J., Boesenberg J.S., Britt D.T., Rivers M.L., Ebel D.S. and Friedrich J.M. 2009. Incompletely compacted equilibrated ordinary chondrites. *Meteoritics & Planetary Science* 44(11): 1743-1753.

Schmieder M., Tohver E., Jourdan F., Denyszyn S.W. and Haines P.W. 2015. Zircons from the Acraman impact melt rock (South Australia): shock metamorphism, U–Pb and 40Ar/39Ar systematics, and implications for the isotopic dating of impact events. *Geochimica et Cosmochimica Acta* 161*:* 71-100.

Schmieder, M., Kring, D.A., Swindle, T.D., Bond, J.C. and Moore, C.B., 2016. The Gao-Guenie impact melt breccia—Sampling a rapidly cooled impact melt dike on an H chondrite asteroid? *Meteoritics & Planetary Science* 51(6): 1022-1045.

Schmitt R.T. 2000. Shock experiments with the H6 chondrite Kernouvé: Pressure calibration and microscopic shock effects. *Meteoritics & Planetary Science* 35: 545-560.

Schmitt R.T. and Stöffler D. 1995. Experimental data in support of the 1991 shock classification of chondrites. *Meteoritics & Planetary Science* 30: 574-575.

Scott E.R., Keil K. and Stöffler D., 1992. Shock metamorphism of carbonaceous chondrites. *Geochimica et Cosmochimica Acta* 56(12): 4281-4293.

Stöffler D., Keil K. and Scott E.R.D. 1991. Shock metamorphism of ordinary chondrites. *Geochimica et Cosmochimica Acta* 55 (12): 3845-3867.

Stöffler D., Hamann C. and Metzler K. 2018. Shock metamorphism of planetary silicate rocks and sediments: Proposal for an updated classification system. *Meteoritics & Planetary Science* 53(1): 5-49.

Stöffler D., Hamann C. and Metzler K. 2019. Addendum to "Stöffler, D., Hamann, C., and Metzler, K., Shock metamorphism of planetary silicate rocks and sediments: Proposal for an updated classification system. Meteoritics & Planetary Science 53, 5–49, 2018". *Meteoritics & Planetary Science* 54(4): 946-949.

Wittmann A., Swindle T.D., Cheek L.C., Frank E.A. and Kring D.A., 2010. Impact cratering on the H chondrite parent asteroid. *Journal of Geophysical Research: Planets* 115(E7).

Wolf S.F., Compton J.R., and Gagnon C.J. 2012. Determination of 11 major and minor elements in chondritic meteorites by inductively coupled plasma mass spectrometry. *Talanta* 100: 276-81.

Yamaguchi A., Scott E.R. and Keil K. 1999. Origin of a unique impact-melt rock—The L-chondrite Ramsdorf. *Meteoritics & Planetary Science* 34(1): 49-59.

Zhang A.C., Wang R.C., Hsu W.B. and Bartoschewitz R. 2013. Record of S-rich vapors on asteroid 4 Vesta: Sulfurization in the Northwest Africa 2339 eucrite. *Geochimica et Cosmochimica Acta* 109: pp.1-13.

Zingg Th. 1935. Beitrag zur Schotteranalyse: Die Schotteranalyse und ihre Anwendung auf die Glattalschotter. *Schweizerische Mineralogische und Petrographische Mitteilungen* 15: 39–140.

Table 1. Number of recognized ordinary chondrite melt breccias*.

Group Type	H	L	LL	Total
3	0	3[2]	0	3 of 3028 (0.10%)
4	8	5	1	14 of 8763 (0.15%)
5	20	20	4	44 of 20141 (0.22%)
6	8	22	7	37 of 19753 (0.19%)
Other[1]	7	19	10	36
Total	43	69	22	134 of 51725 (0.26%)

* Data from Meteoritical Bulletin Database (MBD, 2019), accessed October 9, 2019. Does not take into account possibility of pairing.
[1] Undesignated or multiple types. [2] The three type 3 melt breccias, all L group, are NWA 8709, NWA 7120, and NWA 12547.

Table 2. Average compositions of olivine and pyroxene (±1σ in parentheses) in NWA 8709, based on quantitative EDS map and point data*.

	Primary[1] olivine (map)	Primary[1] olivine (point)	Secondary[2] olivine (point)	Matrix[3] olivine (point)	Primary[1] low-Ca pyroxene (map)	Primary[1] low-Ca pyroxene (point)	Secondary[2] pigeonite (point)	Matrix[3] pigeonite (point)	Matrix[3] low-Ca pyroxene (point)	Matrix[3] augite (point)
N	118	43	13	40	51	33	7	32	14	7
Wt%										
SiO_2	39.3 (0.9)	40.1 (2.8)	37.8 (2.5)	40.4 (1.1)	56.8 (1.4)	56.1 (1.5)	55.0 (0.9)	54.6 (1.1)	56.1 (1.2)	53.1 (0.7)
TiO_2	<0.58	0.02 (0.02)	0.03 (0.03)	0.05 (0.03)	<0.49	0.04 (0.03)	0.12 (0.03)	0.13 (0.03)	0.08 (0.02)	0.33 (0.04)
Al_2O_3	<0.55	0.08 (0.06)	0.10 (0.06)	0.64 (0.41)	0.37 (0.46)	0.35 (0.14)	0.54 (0.24)	1.41 (0.53)	0.95 (0.68)	1.73 (0.48)
Cr_2O_3	0.17 (0.27)	0.20 (0.14)	0.27 (0.08)	0.31 (0.06)	0.40 (0.45)	0.57 (0.17)	0.88 (0.16)	1.00 (0.14)	0.72(0.18)	1.58 (0.11)
FeO	14.3 (3.0)	13.7 (3.8)	23.3 (6.5)	16.2 (1.2)	8.38 (4.22)	10.6 (4.6)	12.3 (2.8)	10.2 (0.9)	8.97 (2.64)	6.69 (0.53)
MnO	0.37 (0.48)	0.44 (0.14)	0.55 (0.16)	0.49 (0.04)	<0.82	0.38 (0.19)	0.51 (0.09)	0.51 (0.06)	0.43 (0.17)	0.41 (0.03)
MgO	44.6 (2.7)	45.3 (3.8)	37.4 (5.4)	41.7 (1.4)	32.6 (5.6)	30.9 (3.5)	26.7 (2.2)	27.5 (1.0)	30.8 (2.9)	20.5 (1.2)
NiO	<0.47	<0.04	b.d.	<0.12	<0.49	<0.20	b.d.	<0.08	0.04 (0.06)	0.06 (0.05)
CaO	0.17 (0.23)	0.15 (0.10)	0.24 (0.06)	0.28 (0.20)	0.78 (0.67)	0.72 (0.57)	3.66 (0.97)	3.62 (0.90)	1.58 (0.70)	14.4 (1.2)
Na_2O	<0.41	0.08 (0.02)	0.12 (0.04)	0.18 (0.07)	<0.43	0.09 (0.04)	0.20 (0.03)	0.35 (0.10)	0.23 (0.15)	0.62 (0.07)
K_2O	<0.27	b.d.	b.d.	<0.04	<0.44	b.d.	b.d.	<0.03	b.d.	<0.03
S	<0.10	0.05 (0.04)	0.04 (0.01)	0.27 (0.31)	<0.10	0.08 (0.02)	0.07 (0.01)	0.24 (0.13)	0.19 (0.15)	0.14 (0.09)
	98.9	100.1	100.2	100.6	99.1	99.9	99.9	99.5	100.1	99.6
Mol%										
Fa	15.3 (3.3)	14.7 (4.1)	26.1 (8.0)	17.9 (1.3)	--	--	--	--	--	--
Wo	--	--	--	--	1.5 (1.3)	1.4 (1.1)	7.3 (2.0)	7.3 (1.9)	3.1 (1.4)	30.0 (2.8)
Fs	--	--	--	--	12.6 (6.8)	16.1 (7.4)	19.1 (4.7)	16.0 (1.3)	13.7 (4.2)	10.9 (0.8)
En	--	--	--	--	85.9 (7.3)	82.5 (7.7)	73.7 (5.0)	76.7 (2.3)	83.2 (5.5)	59.2 (2.3)

* N = number of analyses. b.d. = below detection. Pyroxene categories: low-Ca pyroxene Wo≤5, pigeonite Wo5-15, augite Wo>20. See Supplement for further details.

[1] Primary: coarse (>30 μm across) and/or blackened grains within chondrules or chondrule fragments.

[2] Secondary: fine (<10 μm across), non-blackened grains, within chondrules or chondrule fragments.

[3] Matrix: very fine (typically ≤5 μm across) grains, within melt matrix.

Table 3. Concentrations of 53 elements in NWA 8709 obtained by ICP-MS.

element	Units	concentration
Li	µg/g	2.0
Na	mg/g	6.1
Mg	mg/g	148
Al	mg/g	11.9
Sc	µg/g	8.3
Ti	µg/g	620
V	µg/g	85
Mn	mg/g	2.9
Fe	mg/g	180
Co	µg/g	420
Ni	mg/g	10.0
Cu	µg/g	73
Zn	µg/g	55
Ga	µg/g	5.9
As	µg/g	1.2
Se	µg/g	6.7
Rb	µg/g	3.4
Sr	µg/g	9.4
Y	µg/g	2.5
Zr	µg/g	7.3
Nb	ng/g	470
Mo	µg/g	1.4
Ru	µg/g	1.1
Pd	ng/g	560
Ag	ng/g	420
Sn	ng/g	380
Sb	ng/g	90
Te	ng/g	290
Cs	ng/g	310
Ba	µg/g	20.2
La	ng/g	375
Ce	ng/g	987
Pr	ng/g	147
Nd	ng/g	679
Sm	ng/g	231
Eu	ng/g	82
Gd	ng/g	305
Tb	ng/g	61
Dy	ng/g	318
Ho	ng/g	79
Er	ng/g	231
Tm	ng/g	39
Yb	ng/g	223
Lu	ng/g	41
Hf	ng/g	170
Ta	ng/g	14
W	ng/g	110
Re	ng/g	50
Ir	ng/g	500
Pt	ng/g	830
Bi	ng/g	19
Th	ng/g	52
U	ng/g	16

Table 4. Whole rock oxygen isotope analysis results for NWA 8709.

Sample	$\delta^{17}O$ (‰)	$\delta^{18}O$ (‰)	$\Delta^{17}O$ (‰)	$\Delta^{17}O$ (‰) linear
0109-1[1], 2.3 mg	3.482	5.033	0.865	0.842
0109-7[2], 1.5 mg	3.342	4.851	0.819	0.781
0109-7[2], 1.6 mg	3.388	5.099	0.737	0.696
0109-7[2], 2.7 mg	3.315	4.348	0.874	0.839
Mean ± 1σ	3.337 ± 0.147	4.833 ± 0.340	0.824 ± 0.063	0.789 ± 0.068

[1]Sample CML0109-1, untreated, analyst Richard Greenwood.
[2]Sample CML0109-7, acid-treated to remove terrestrial weathering products, analyst Karen Ziegler.

Table 5. Physical properties of NWA 8709 (sample CML0109-5C, microtomography performed before pycnometry).

Mass	2.34 g
Bulk volume[1]	0.69 ± 0.04 cm^3
Bulk density[2]	3.39 ± 0.20 g/cm^3
C[3]	0.68
Mass	2.16 g
Grain volume[4]	0.64 ± 0.01 cm^3
Grain density	3.35 ± 0.05 g/cm^3
Bulk volume[5]	0.67 ± 0.01 cm^3
Bulk density[6]	3.22 ± 0.05 g/cm^3
Porosity[7]	4.1 ± 2.1%

[1] Determined by microtomography.
[2] Determined by mass and microtomography.
[3] Metal grain orientation strength factor (shape preferred orientation), determined by microtomography.
[4] Determined by ideal gas pycnometry.
[5] Determined by laser scanning.
[6] Using mass and laser-scanned bulk volume.
[7] Using bulk and grain densities as determined by pycnometry and laser scanning.

Table 6. Chondrule diameters in NWA 8709, determined by optical microscopy (2D) in sections CML0109-2 and CML0109-5D, and by microtomography (3D, equivalent diameter*) in sample CML0109-5C.

	N	normal ($\bar{x}$ ± 1σ, µm)	log-normal ($\bar{x}$ ± 1σ, µm)
2D	53	830 ± 380	
3D	156	940 ± 340	890 +340/-240

* Equivalent diameter is the diameter of a sphere corresponding to the measured volumes.
N = number of chondrules.

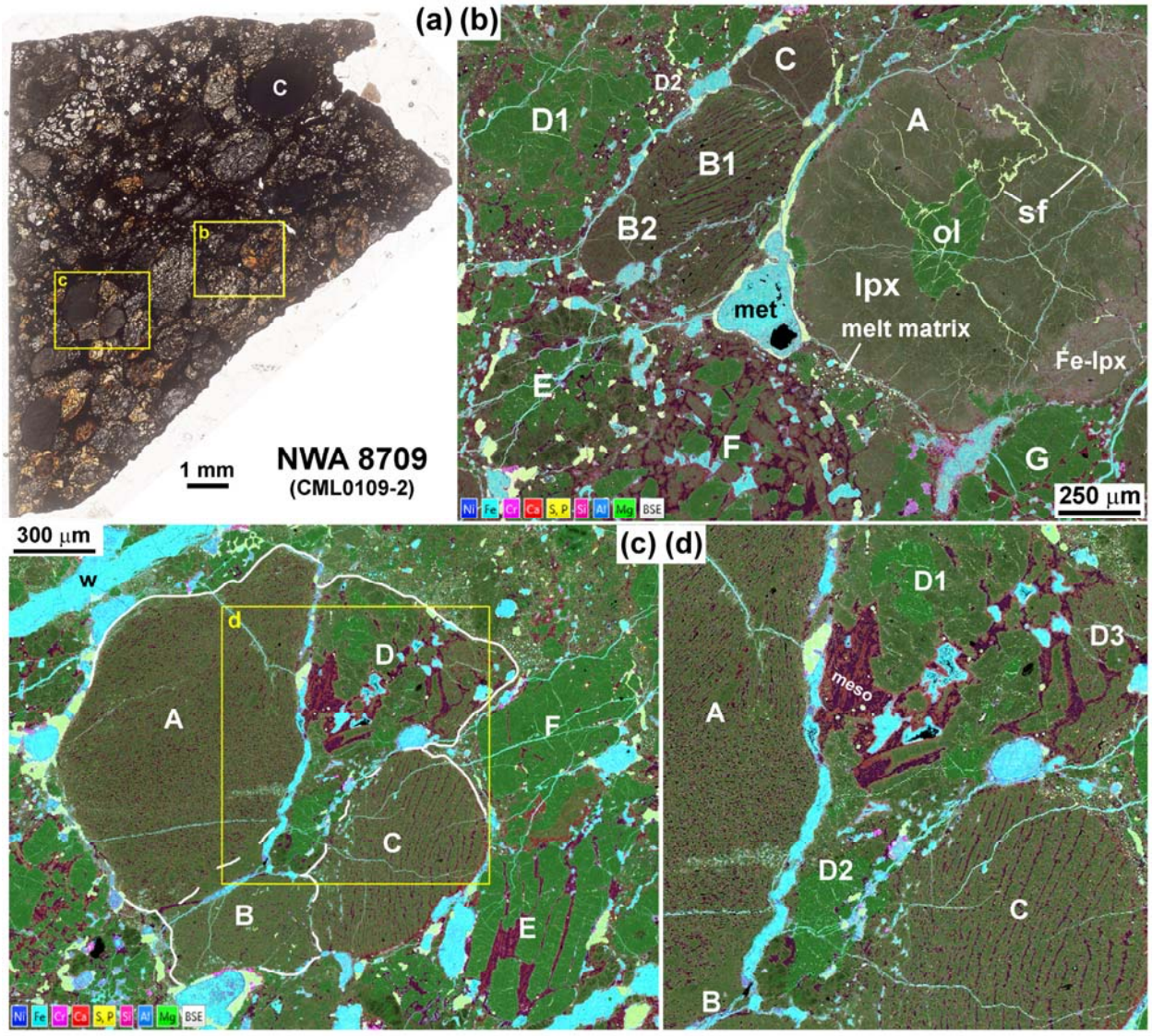

Fig. 1. Large scale features of NWA 8709 as seen in thin section. **(a)** Transmitted light micrograph of sample CML0109-2, showing chondrules and overall dark appearance caused mainly by fine metal-sulfide grains ("blackening"). Chondrules have a preferred shape alignment of long axes (lower left - upper right). The box indicates the field-of-view of parts (b) and (c), and "C" indicates one of the larger chondrules, a cryptocrystalline chondrule (apparent length ~1.8 mm) that is dark owing to fine grain size and not to blackening. Other large chondrules are visible. **(b)** Enlarged view from part (a) showing false color EDS+BSE image, where colors represent X-ray emission intensity (K-alpha peak counts) for different elements and overall brightness represents BSE image brightness. Chondrules (A, B1/B2, C, D1/D2, E, F, G) are closely spaced and separated by melt matrix or sulfide-metal veins. Phase colors: olivine (ol) = green; low-Ca pyroxene (lpx, orthopyroxene, clinoenstatite) = brown (magnesian) to tan (ferroan); pigeonite (not readily visible here) = reddish tan; high-Ca pyroxene (augite, visible in

F) = red; weathered metal (met) or metal = light blue; sulfide (sf) = greenish-yellow; feldspathic material (mostly glass, examples in D2, E, F, G) = purple; chromite = fuschia; black = voids (most prominent within the largest weathered metal at center). A large pore (black) occurs in the accumulation of weathered metal near the center. Chondrule features: sf veins in pyroxene-olivine chondrule A occur mostly in ol and Mg-lpx, less so in Fe-lpx towards edges of chondrule where they transition into feldspathic glass veins; chondrule B is a composite object with a larger barred olivine-pyroxene region (B1) with bent ol bars, and a smaller pyroxene-rich, cryptocrystalline region (B2); cryptocrystalline, pyroxene-rich chondrule C is molded against B1; chondrule D has an olivine-rich microporphyritic core (D1) that grades into a fine-grained, granular rim (D2) and into melt matrix. **(c)** Enlarged view from part (a) showing false color EDS + BSE image (colors same as part b). Chondrules (A, B, C, D, E, F) are closely spaced, with A-D forming an especially tight cluster. Yellow box shows area enlarged in part d. **(d)** Closer view from part c. Chondrules A, B and C are fine-grained pyroxene-rich chondrules that are largely unblackened by sulfide; microporphyritic chondrule D has blackened olivine and pyroxene phenocrysts in regions D1 and D2 but not in D3, as well as an unblackened mesostasis (meso). w = vein filled with weathering products. See Text for additional explanation.

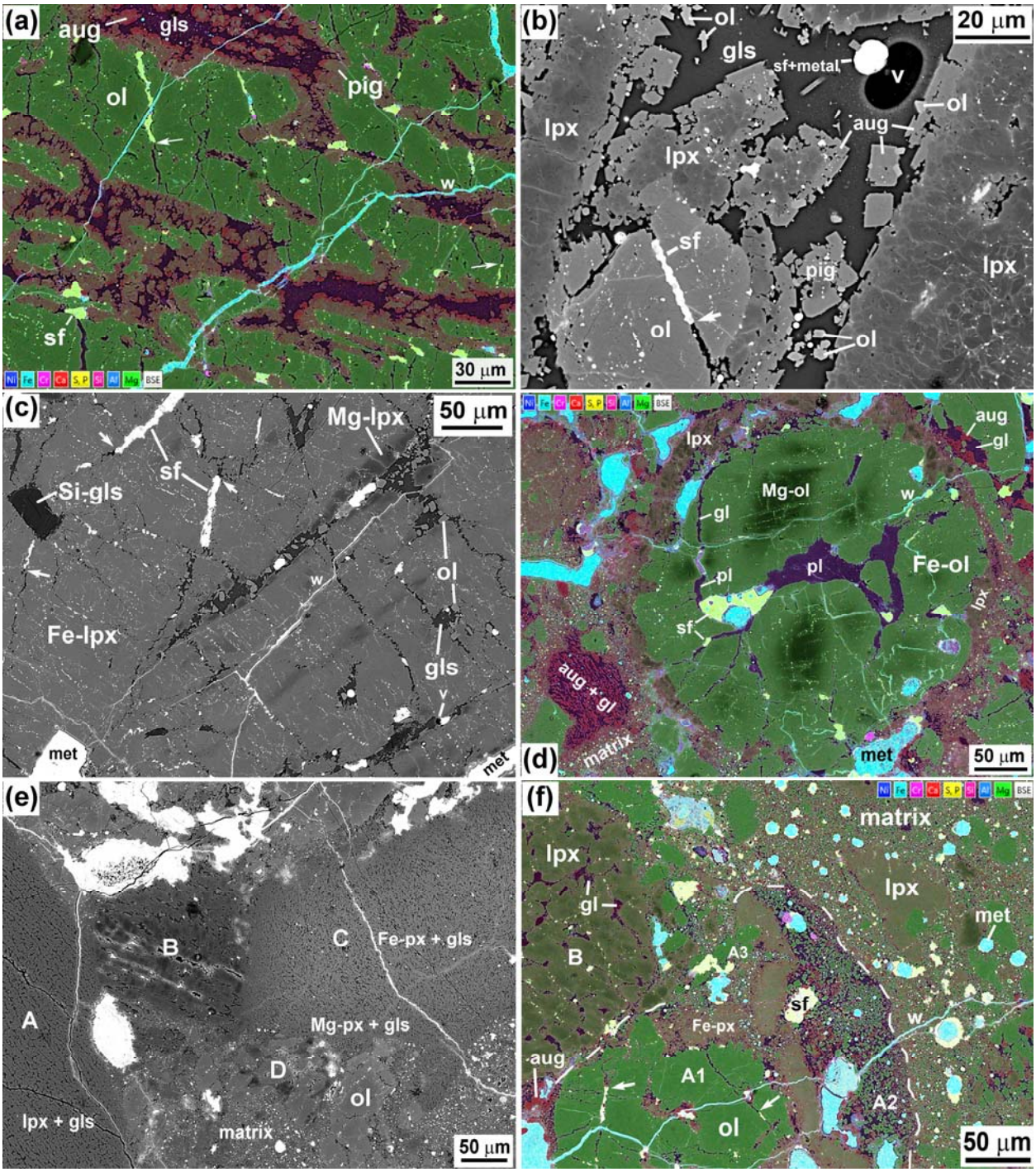

Fig. 2. Chondrule features of NWA 8709 as seen in thin section. **(a)** False-color EDS+BSE image (colors and phases same as Fig. 1b) showing interior of microporphyritic chondrule containing olivine (ol) phenocrysts overgrown with pigeonite (pig) and augite (aug) set in feldspathic glass (gls). Sulfide (sf) inclusions and veins (some of which grade into gls veins, at arrows) cross-cut ol phenocrysts but not other phases. Weathering veinlets (w) cross the region. Sample CML0109-5D. **(b)** BSE image of microporphyritic chondrule containing olivine (ol) and

low-Ca pyroxene (lpx) phenocrysts, overgrown with augite (aug) and fine-grained ol, all set in feldspathic glass (gls) mesostasis. Sulfide (sf) inclusions and veins (white) are concentrated in ol and lpx phenocrysts and absent in aug and ol overgrowths; one thick sf vein grades into gls (arrow). A prominent vesicle (v) occurs in the glassy mesostasis, adjacent to a sulfide + metal globule that partly projects into the void. Sample CML0109-2. **(c)** BSE image of interior of a microporphyritic pyroxene chondrule that contains grain cores of ferroan low-Ca pyroxene (Fe-lpx) and rims of magnesian low-Ca pyroxene (Mg-lpx), set in mesostasis of feldspathic glass (gls) and silica glass (Si-gls). Numerous sulfide (sf) inclusions and veins occur in the Fe-lpx; sf veins grade into gls veins (arrows). Small vesicles (v, lower right) occur in the glass mesostasis. Minor weathering veinlets (w) occur in the chondrule. Sample CML0109-2. **(d)** False-color EDS+BSE image (colors and phases same as Fig. 1b) showing a microporphyritic chondrule, which contains olivine phenocrysts strongly zoned with magnesian cores (Mg-ol) and ferroan portions (Fe-ol), both of which contain sulfide inclusions; a rim of low-Ca pyroxene (lpx) surrounds the chondrule. Plagioclase (pl) occurs between ol in the center of the chondrule and in veins that extend outward into feldspathic glass (gls) and mixtures of sulfide (sf) and metal.The chondrule is surrounded by melt matrix. Nearby chondrules and fragments contain augite (aug) and gls; the fragment at left resembles chondrule mesostasis. Weathering veinlets (w) cross the area. Sample CML0109-5D. **(e)** BSE image of three attached, pyroxene-rich chondrules (A, B, C), surrounded by melt matrix and small chondrule fragments (D) containing olivine (ol) phenocrysts. Cryptocrystalline chondrule A is composed chiefly of low-Ca pyroxene (lpx) and feldspathic glass (gls) and notably lacks sulfide inclusions and veins; it is representative of larger chondrules (in this case, ~1.4 mm in apparent diameter) of this type. Cryptocrystalline chondrule C is composed chiefly of lpx, pigeonite, and gls, and is zoned from a more ferroan core (Fe-px + gls) to a more magnesian rim (Mg-px + gls). Irregular lines are cracks partly filled with weathering product. Sample CML0109-5D. **(f)** False-color EDS+BSE image (colors and phases same as Fig. 1b) showing chondrules and adjacent melt matrix. Metal (met) – sulfide (sf) globules and patches are prominent in matrix but also occur in chondrules. At left is a microporphyritic chondrule (B) containing phenocrysts of low-Ca pyroxene (lpx) set in glass (gl); sulfide inclusions form lines that cross-cut the lpx. Another chondrule (dashed line) contains different regions. This includes a microporphyritic region (A1) that contains phenocrysts of olivine (ol) cross-cut by sulfide-glass veins (arrows), and phenocrysts of ferroan low-Ca pyroxene and pigeonite (Fe-px) that lack such veins; another region (A2) that is fine-grained and texturally distinct from melt matrix, consisting of euhedral-subhedral olivine, pigeonite, and augite set in feldspathic glass; and another region (A3) that contains fine-grained material and olivine clasts that resembles adjacent melt matrix. Weathering veinlets (w) cross-cut matrix and chondrules. See Text for additional explanation. Sample CML0109-2.

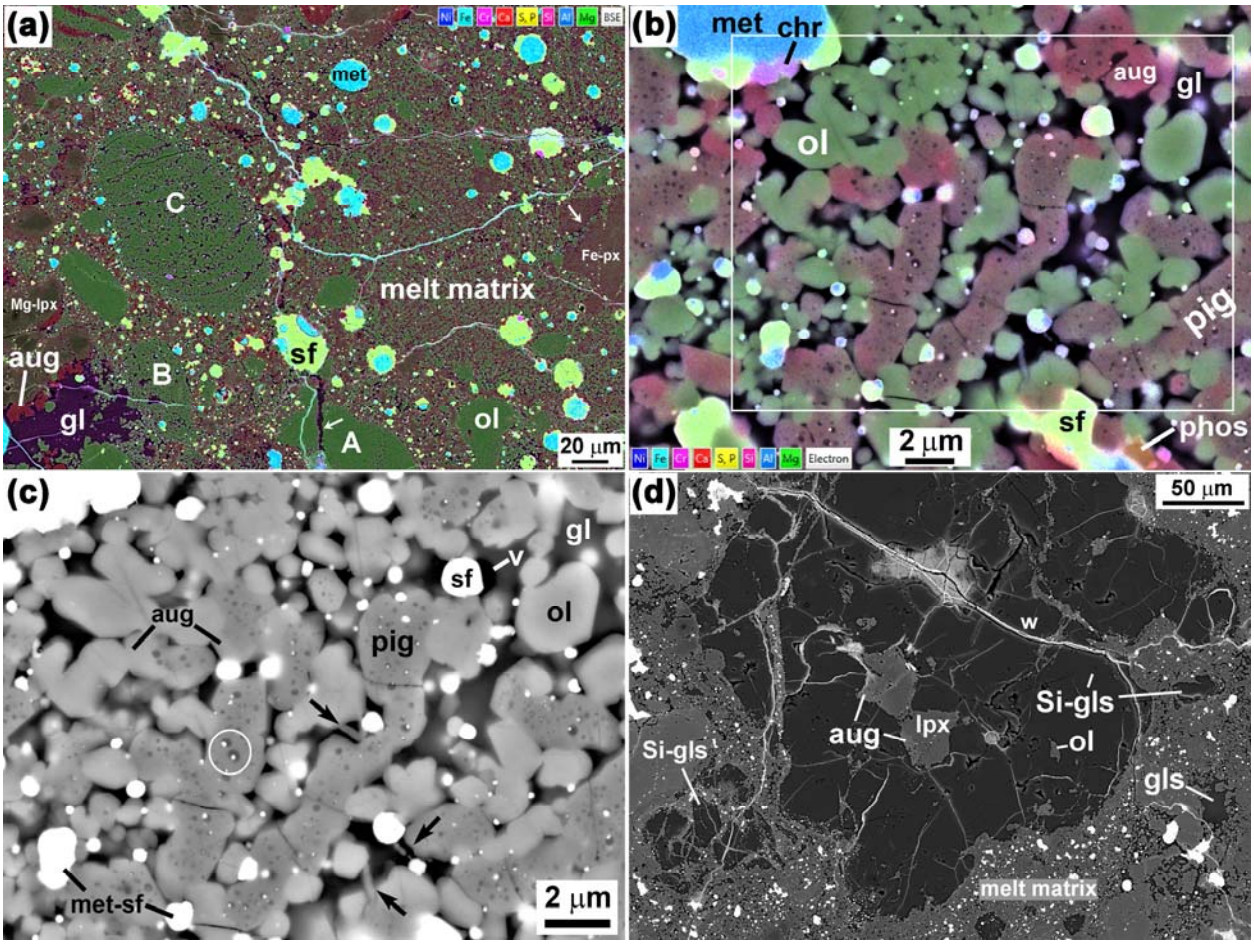

Fig. 3. Matrix features of NWA 8709 as seen in thin section. **(a)** False-color EDS+BSE image (colors and phases same as Fig. 1b) showing typical region of melt matrix, composed of fine-grained (≤5 μm) silicates, metal (met) – sulfide (sf) globules, and lithic clasts. The latter in this area include fine-grained, olivine (ol)-rich clasts (A, B, C); a chondrule remnant (lower left) composed of magnesian low-Ca pyroxene (Mg-lpx), augite (aug) overgrowths, and feldspathic glass (gls); and a pyroxene-rich clast (right, ferroan low-Ca pyroxene to pigeonite, Fe-px). A gls vein (arrow, bottom) cross-cuts clast A and adjacent matrix and extends to a prominent met-sf nodule, and a vein of gls + fine-grained ol (arrow, right) cross-cuts Fe-px and grades into melt matrix. Sample CML0109-5D. **(b)** False-color EDS+BSE image (colors and phases same as Fig. 1b) showing a close-up of matrix, which consists chiefly of pigeonite (pig), olivine (ol), augite (aug) and globules of sulfide (sf) and metal (met) set in feldspathic glass (gl). In close spatial association with met and sf are phosphate (phos, orange) and chromite (chr). The box shows the region enlarged in part (c). Sample CML0109-2. **(c)** Slightly enlarged BSE image of matrix from part (b) with brightness and contrast optimized to show the presence of voids (v, black) within glassy groundmass (gl, dark grey), and elongate crystals that bridge the voids (arrows). Except for the void marked v, most voids seen here are present at the surface only, and do not penetrate very deep into the section. Metal-sulfide (met-sf) globules occur interstitial to silicates. Pigeonite is rich in tiny (≤0.4 μm-across), multiphase inclusions composed of glass with smaller blebs of sf and met (example circled). Augite (aug) forms overgrowths on pigeonite. **(d)** BSE image

showing patches of Si-rich glass (dark grey, Si-gls) in matrix, including here the largest compact patch found in NWA 8709. Si-gls is chemically distinct from nearby feldspathic glass (dark grey, gls), and is intergrown with vein-like extensions of matrix, with the large patch also containing occasional grains of olivine (ol) and composite grains of low-Ca pyroxene (lpx) and augite (aug). Weathering veinlets (w) cross-cut both matrix and Si-gls. See Text for additional explanation. Sample CML0109-5D.

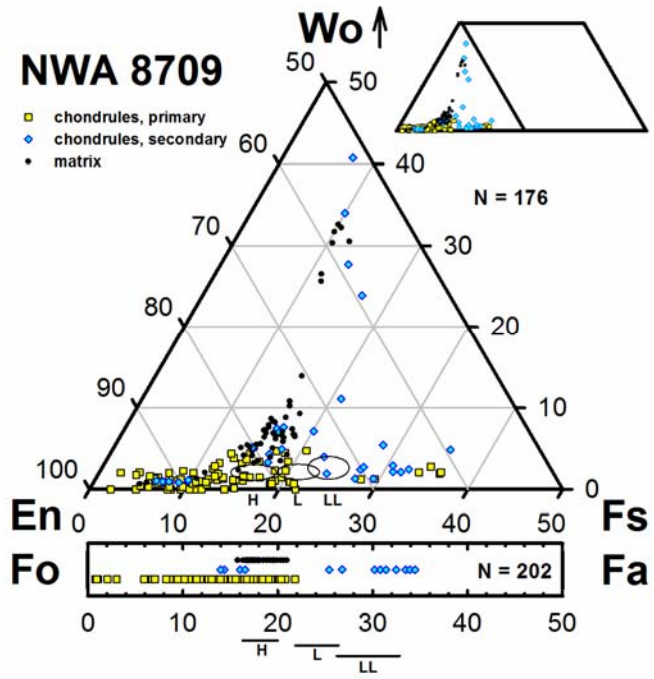

Fig. 4. Portion of pyroxene quadrilateral and an olivine plot showing the composition of pyroxene and olivine in NWA 8709, compared to that in H4-6, L4-6, and LL4-6 chondrites (Brearley and Jones, 1998; Grossman and Rubin, 2006). Yellow squares represent coarse chondrule ("primary") phases, often blackened by sulfide; light blue diamonds represent fine-grained, non-blackened chondrule ("secondary") phases; and black dots represent fine-grained matrix phases. N = number of analyses. Fo = mol% forsterite and Fa = mol% fayalite in olivine; En = mol% enstatite, Fs = mol% ferrosilite, and Wo = mol% wollastonite in pyroxene.

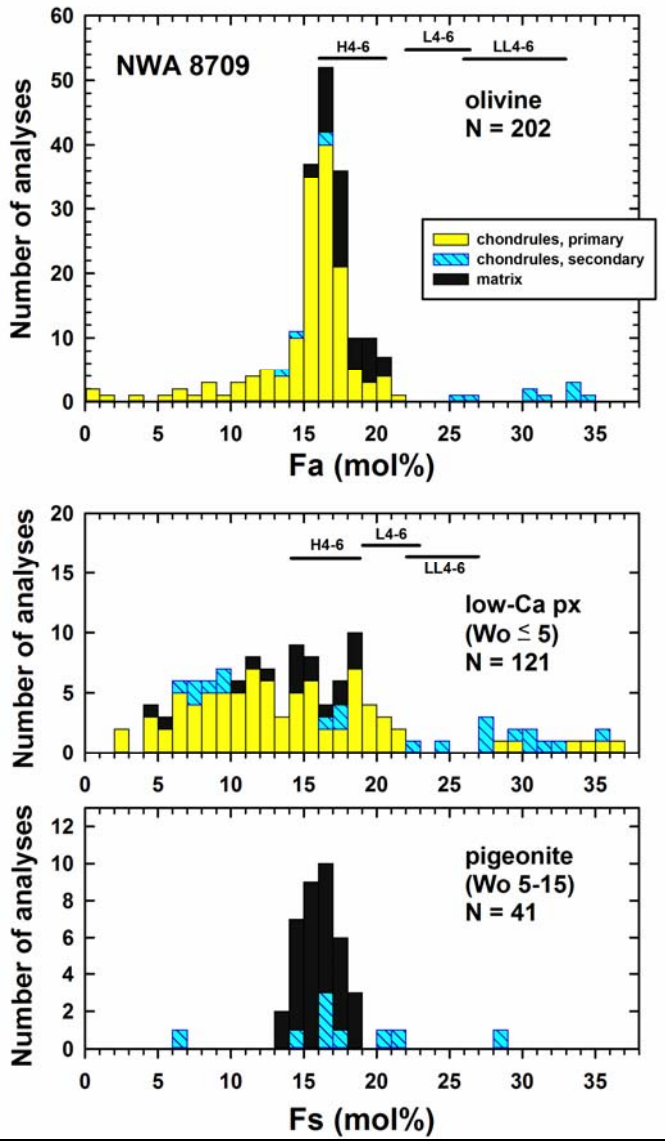

Fig. 5. Distribution of Fa (mol% fayalite) in olivine and Fs (mol% ferrosilite) in low-Ca pyroxene (px) and pigeonite from NWA 8709, compared to olivine and low-Ca px in H4-6, L4-6, and LL4-6 chondrites (Brearley and Jones, 1998; Grossman and Rubin, 2006). Yellow bars represent coarse chondrule ("primary") phases, often blackened by sulfide; light blue ruled bars represent fine-grained, non-blackened chondrule ("secondary") phases; and black bars represent fine-grained matrix phases. N = number of analyses.

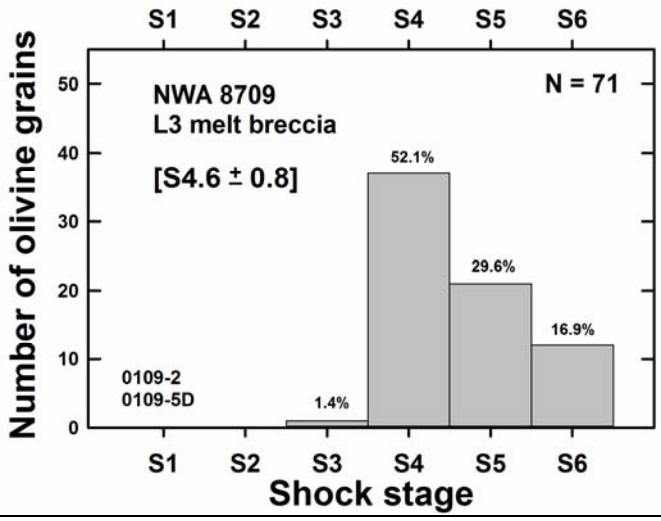

Fig. 6. Distribution of shock stages for olivine in NWA 8709, as determined by optical microscopy using the method of Jamsja and Ruzicka (2010). Weighted shock stage is shown in brackets. N = number of grains.

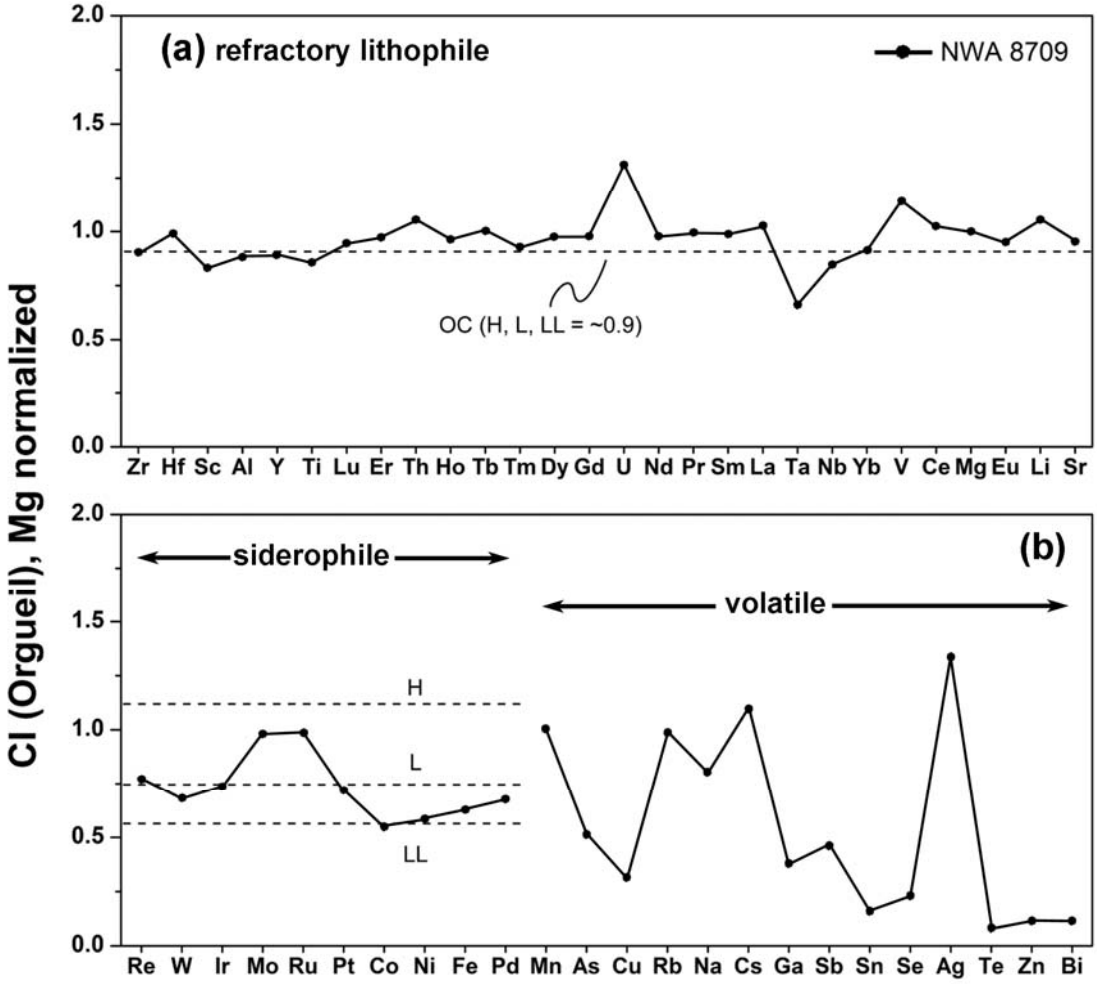

Fig. 7. CI-chondrite and Mg-normalized abundances of 52 elements in NWA 8709. **(a)** Refractory lithophile element abundances. The dashed line indicates the typical ~0.9 refractory lithophile abundances for ordinary chondrites (OC) (Kallemeyn et al., 1989). **(b)** Refractory siderophile element abundances (Re-Pd), and moderately volatile element abundances (Mn-Bi). The dashed lines for siderophile elements indicate the typical abundances found for H, L, and LL chondrites (Kallemeyn et al., 1989).

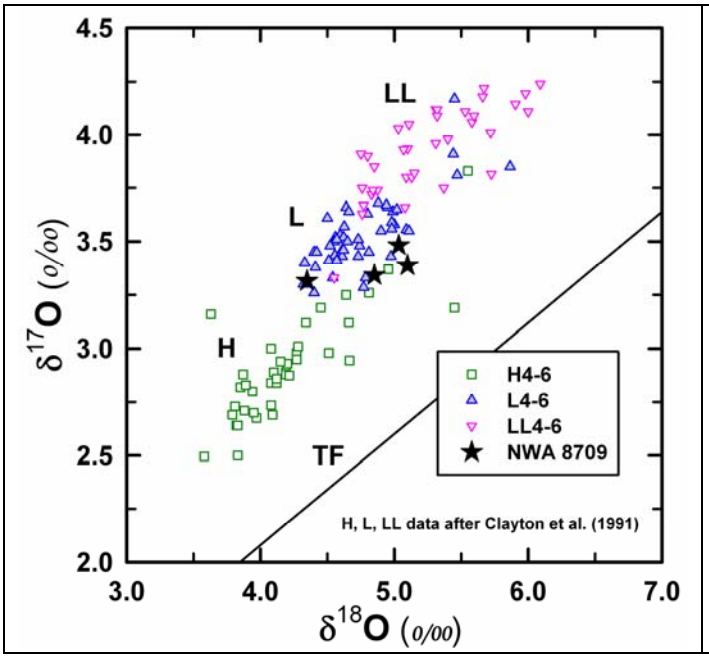

Fig. 8. Oxygen isotope composition of NWA 8709, compared to H4-6, L4-6 and LL4-6 chondrites (Clayton et al., 1991). TF = terrestrial fractionation line. Data for NWA 8709 are most consistent with L chondrites.

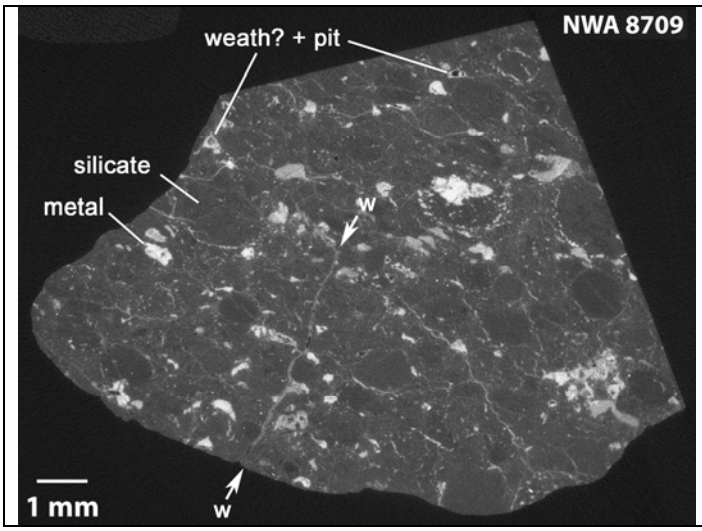

Fig. 9. A tomogram of NWA 8709. Brightness decreases as follows: metal, sulfide and metal weathering product (which are difficult to distinguish), silicate, and air (surrounding the rock and pores within it). Chondrules can be recognized. "w" indicates a vein largely filled with (apparent) weathering product and containing some voids; other voids or pits are associated with likely weathering (weath?) product.

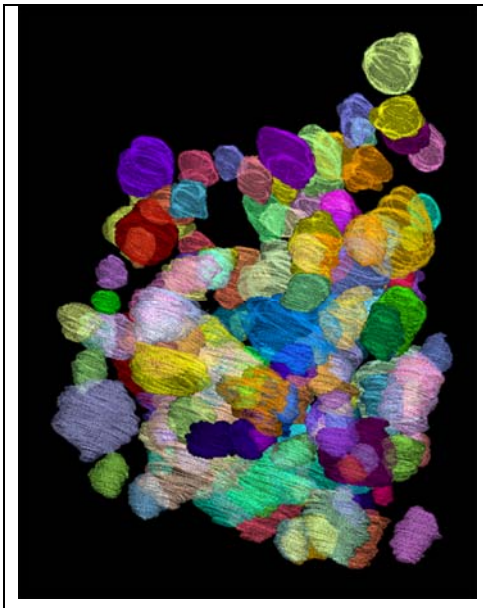

Fig. 10. 3D representation of 156 digitally marked individual chondrules in NWA 8709. The non-spherical, somewhat lumpy nature of the chondrules is apparent.

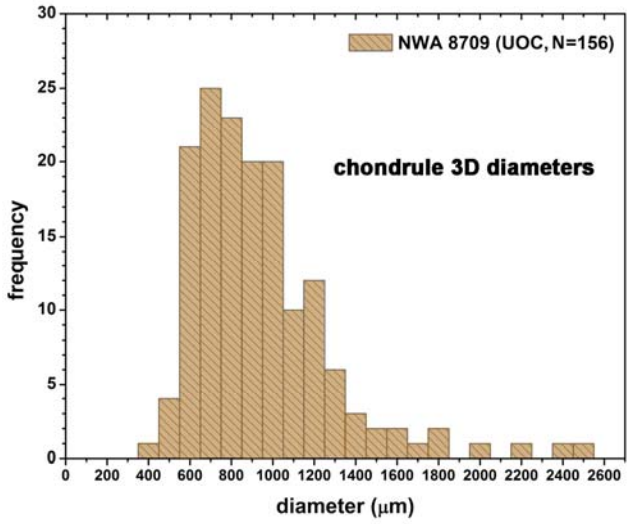

Fig. 11. Histogram of effective chondrule diameters in the NWA 8709 unequilibrated ordinary chondrite (UOC) based on 3D microtomography data. Most chondrules have effective diameters of ~600-1000 μm, though the largest range to ~2500 μm. These sizes are most consistent with LL chondrites (Friedrich et al., 2015).

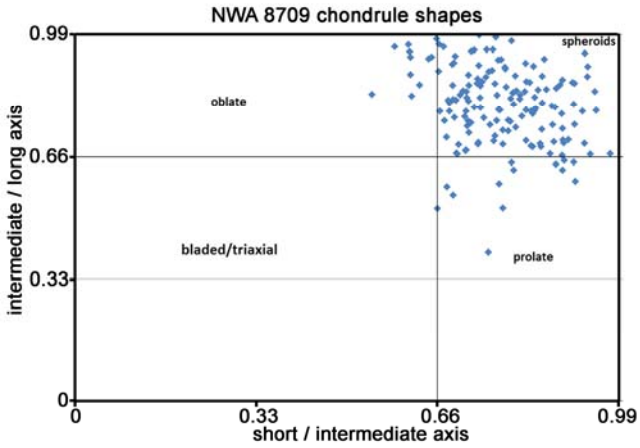

Fig. 12. Shapes of chondrules in NWA 8709, using the Zingg (1935) system of shape classification. This system uses the long, intermediate, and short axes of the best fit ellipsoid of the particle to classify the shapes of particles into one of four overall types. Most chondrules in NWA 8709 are relatively equant and fall into the "spheroid" field of Zingg.

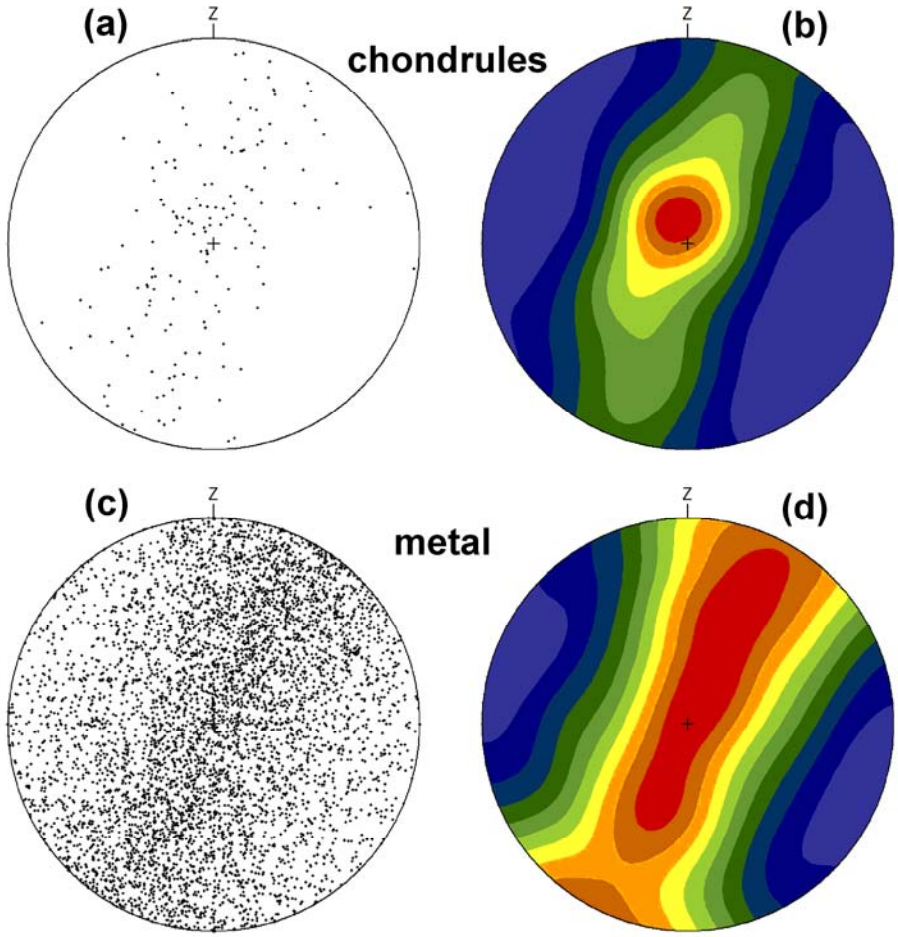

Fig. 13. Stereographs for particle shape orientations in NWA 8709, based on microtomography data. **(a)** The long axes of 156 chondrules. **(b)** A spatial density representation based on part (a) of collective chondrule orientation (red = most frequent, blue = least frequent). **(c)** The long axes of 5655 metal grains. **(d)** A spatial density representation based on part (c) of collective metal grain orientation. The shape orientations of chondrules and metal grains show a similar pattern, consistent with a common foliation produced by compaction (upper left -- lower right compression direction).

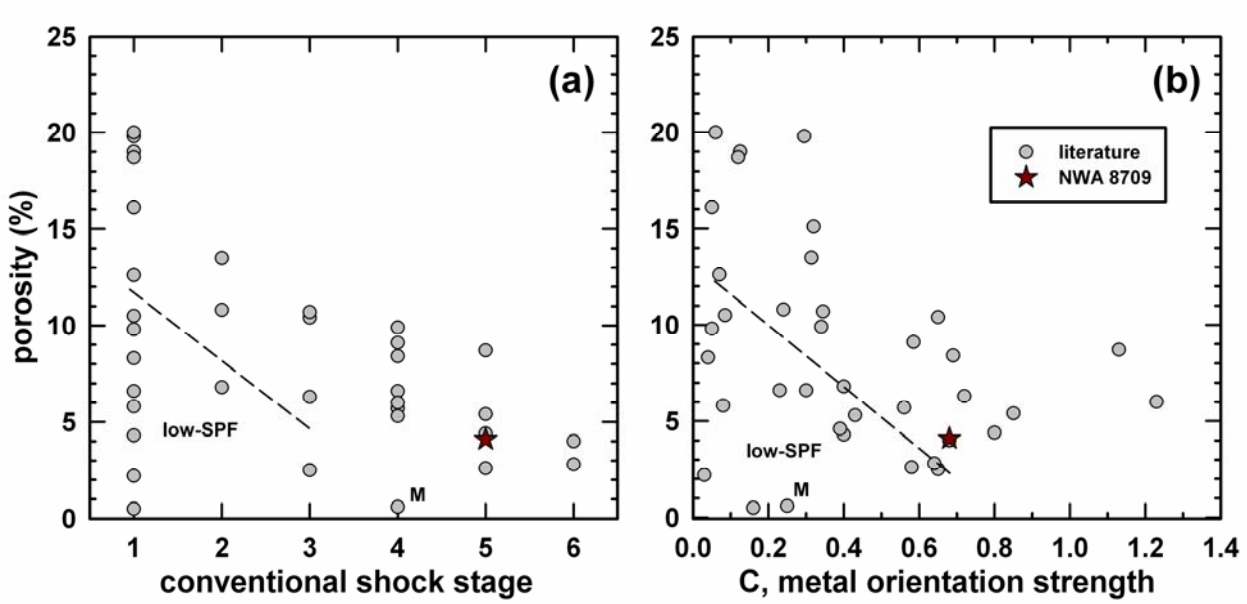

Fig. 14. Relationship between porosity and **(a)** conventional shock stage (Stöffler et al., 1991) and **(b)** metal grain orientation strength C, for NWA 8970 (this work) and other ordinary chondrites (Friedrich et al., 2017; M = MIL 07273, Ruzicka et al., 2017). The dashed lines are guidelines for the approximate field (below the lines) of low-SPF (shock-porosity-foliation) chondrites (Friedrich et al., 2017). NWA 8709 is a non-low-SPF chondrite, as it has a combination of relatively high shock stage and high degree of metal grain preferred orientation, with an appropriate porosity.

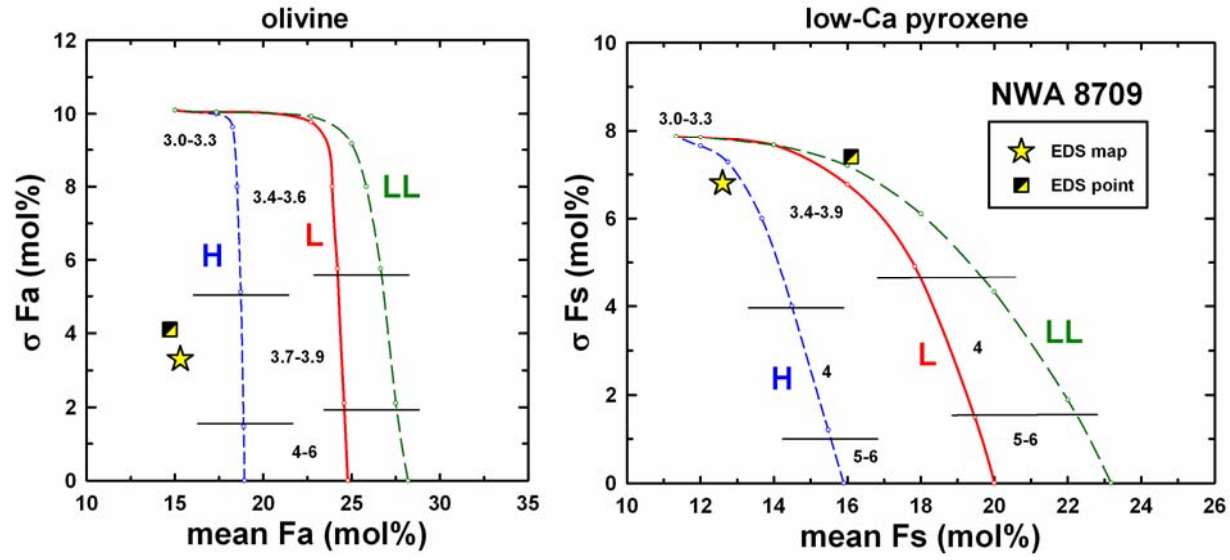

Fig. 15. Mean composition and standard deviation (σ) of Fa (mol% fayalite) in olivine and Fs (mol% ferrosilite) in low-Ca pyroxene from coarse chondrule phases in NWA 8709, obtained with EDS map (star) and EDS point (half-shaded squares) data (Table 2), compared to observed metamorphic compositional tracks in H, L, and LL chondrites (Grossman, 2011). Numbers by H, L, and LL tracks represent type and subtype designations, black horizontal lines approximate boundaries between these. Phase compositions for NWA 8709 lie significantly off the expected L chondrite track for both olivine (based on both EDS map and point data) and low-Ca pyroxene (EDS map data only, but such data are more numerous and representative).